Calibration of the Sun Sensor

M. G. Tomasko
February 25, 2000

Table of Contents

Table of Tables

Table of Figures

1.0 Introduction

This document describes the calibration of the sun sensor on the Descent Imager/Spectral Radiometer (DISR) instrument for the Huygens Probe of the Cassini Mission. Specifically, here we describe in detail the calibration results for instrument SN03, the flight model that will enter Titan's atmosphere in 2004. The results for field test unit SN02 will be given separately in an appendix.

The purpose of the sun sensor is threefold. Firstly, it must determine the time the probe crosses the azimuth of the sun on each rotation to determine the time and azimuth relative to the sun at which data from the other DISR optical sensors are collected during the descent into Titan's atmosphere. Secondly, the zenith angle of the sun must be determined on each rotation. This permits observations to be corrected during ground processing for changes in the attitude of the probe during the descent. Finally, the sun sensor reports the brightness of the direct solar beam near 945 nm on each of the some 500 rotations of the probe to permit a direct determination of the extinction optical depth above the probe throughout the descent at some ten times greater vertical resolution than is available from our other optical sensors.

The sun sensor consists of an imaging optical system, a reticle consisting of three slits in the focal plane, a narrow band interference filter, and a silicon detector as shown in Fig. 1. Hardware is included to sample the signal from the detector, compare the signal to a

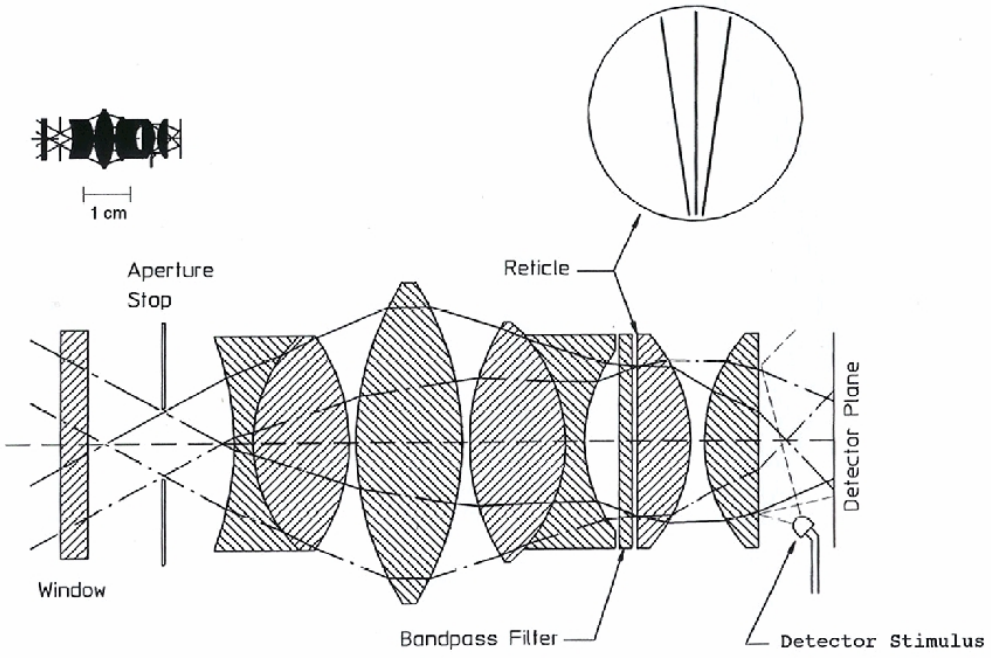

Fig. 1 The schematic layout of the sun sensor. The three-slit reticle is deposited on the front of one of the plano-convex lenses next to the bandpass filter. The size of the optical elements are shown to scale in the upper left corner

with a bar to indicate a size of 1 cm. The detector stimulus is used to inject pulses of light into the system to test functionality during cruise.

threshold value, and determine the time the signal crosses the threshold value in a rising and falling sense for each of the three slits. The mean times of the rising and falling crossings for each of the three slits is determined for each rotation of the probe. The threshold value is dynamically updated based on the maximum value of the signal on the last rotation. Software is included to reject signals from passing clouds by comparing the relative spacing of triplets of pulses. The basic data set from the sun sensor consists of the mean times the sun crossed each of the three slits as well as a number proportional to the flux in the in the center sun sensor slit at 945 nm for each rotation of the probe. We show below that for all cases expected in Titan's atmosphere the direct solar beam dominates the contribution from the diffuse intensity integrated over the slits.

The sun sensor reports no data unless valid sun pulses are observed. Hence, unless a breakout box is used to collect the direct signal from the silicon detector in the sensor head, a dynamical stimulation of the sun sensor must be achieved to read out sun sensor data from the complete instrument. We developed a system that uses a lamp, a collimator, and a rotating flat mirror to sweep a well collimated beam of light past the input of the sun sensor to simulate observations at various rotation rates between 1 and 25 rpm throughout the full zenith angle range (about 25 to 75 degrees) of the instrument.

The calibration of this dynamical system is complex and can be divided into several different portions. The linearity and bias of the transfer function of the detector and electronics must be determined. The absolute responsivity of the system at a standard rotation rate and zenith angle must be determined. The variation of the responsivity with zenith angle and rotation rate must be measured. Any change in the responsivity of the system with temperature must be determined. The response of the system to diffuse light as well as the collimated beam from the sun must be determined. The locations of the slits must be mapped, and an algorithm developed for computing the zenith angle of the sun in the DISR coordinate system in terms of the times of the three slit crossings and the rotation period of the probe. The relative spectral response of the system must be determined. Separate sections of this report are devoted to each of these functions. We begin by describing the transfer function measurements and the absolute calibration of the sun sensor. We conclude by describing the software tests used to discriminate between pulses from the sun and pulses that might result from local cloud structures.

2.0 Linearity and Bias of the Sun Sensor Output Flux Signal

The sun sensor on SN03 was stimulated using the rotating mirror and the collimator at a rotation rate of 4 rpm and at a zenith angle of 50 degrees on September 5, 1996. A series of neutral density filters was used with an aperture at the focus of the collimator to control the brightness and degree of collimation of the beam that was swept past the instrument. Observations were made with two different apertures. One aperture was circular with a diameter of 0.25 inches, and the other was a square 0.6 inches on each

side. For the collimator mirror focal length of 72 inches, the 0.25 inch round aperture produced a beam collimated to 0.2 degrees full width, while the 0.6 inch square aperture produced a beam collimated to 0.48 degrees. The slits of the sun sensor are about 0.25 degrees wide, and so not all the light from the square aperture passed through the sun sensor system. A study of the design of the optical system below indicates the fraction of the light from each aperture that passed through the sun sensor slits.

Several rotations (10 to 15) of the source were observed from the series of neutral density filters for each of the two apertures. Table 1 shows the average and standard deviations of the sun sensor data numbers (DN) observed as well as the signal current from a standard laboratory silicon detector covered with a narrow bandpass filter that used a small pick-off mirror to observe the collimated beam. The bandpass of the filtered standard detector was close to the bandpass of the sun sensor.

The rotating plate that sweeps the collimated beam past the sun sensor has a flat mirror on each side. This gives two signals for each rotation of the plate, with a reflection from each of the two flat mirrors. The reflectivities of the two mirrors are slightly different, and the ratios of the reflectivities of the mirrors are slightly different at the wavelength of the sun sensor and the wavelength of the filtered standard detector. The data in Table 1 are given separately for the signal from the two flat mirrors.

The data were reduced as follows. Note that the brightest signal with the large square aperture (at 4018 and 4019 DN) had an unusually small standard deviation, and is not consistent with the trend of DN with standard detector reading at weaker signal levels. This indicates that the signal was saturated in this case, and this observation was eliminated from further analysis. All other readings, at DN 3500 or less, did not show this effect. Thus, the sun sensor signal may depart from linearity above this level. Fortunately, we show below that we do not anticipate signals above 3500 DN during Titan entry.

A few other measurements were excluded from further reductions. The signal from the brighter side of the mirror using the small aperture and the 0.8 neutral density filter seemed anomalously noisy, and not in good agreement with the trend of the other measurements. This value was eliminated from the analysis. Finally, due to quantization errors, the bright/dark ratio using the 2.5 neutral density filter with the large aperture was not included in the determination of the average bright/dark ratio for the sun sensor. With the elimination of the bright/dark ratios shown in italics in the table, an average bright/dark side mirror ratio of 1.0056 was found for the sun sensor observations. The average bright/dark ratio for the reference detector was found as 1.0088. The darker observations were multiplied by these ratios and averaged with the readings from the brighter side of the mirror to give the last two columns in the table.

A small bias in data number is expected from the design of the sun sensor electronics. This was estimated from the two smallest readings using the large aperture as 2.5 DN. The observed DN-2.5 are plotted versus silicon reference detector current in Fig. 2. The curves are quite linear with two different slopes. A smaller slope for the larger aperture is expected because not all the light from the large aperture is expected to pass through the slits of the sun sensor. The slopes indicate that the ratio of efficiencies of the large and small apertures is 0.5576. With this scaling of the reference signal for the large aperture observations, Figure 3 shows (DN-2.5) for the both apertures plotted versus the scaled silicon reference signal.

Figure 4. shows the residuals from the linear fit to the observations plotted in Fig. 2. The residuals are reasonably balanced around zero, and generally increase as the sun sensor signal increases. The fractional residuals are plotted against sun sensor signal in Fig. 5. The fractional residuals are relatively constant with sun sensor signal, and demonstrate that the sun sensor transfer function is linear to about 1% over its dynamic range.

Table 1
Observations from Linearity Test

Small Aperture	Brighter Side			Darker Side						
		StDev			StDev		Brighter/Darker		Averages scaled to bright side of mirror	
nd	DN	(DN)	Si(amps)	DN	(DN)	Si(amps)	Dn	Si	DN	Si
0	1759.7	2.73	6.460E-07	1747.0	3.74	6.397E-07	1.0073	1.0098	1758.25	6.458E-07
0.3	949.3	1.86	3.535E-07	942.3	1.89	3.501E-07	1.0074	1.0097	948.45	3.534E-07
0.5	568.4	1.72	2.109E-07	565.3	1.21	2.088E-07	1.0055	1.0101	568.44	2.108E-07
0.8	*354.7*	*2.87*	1.112E-07	304.0	0.63	1.102E-07	*1.1668*	1.0091	*305.71*	1.112E-07
1	198.2	0.75	7.180E-08	196.4	0.79	7.120E-08	1.0092	1.0084	197.85	7.182E-08
1.3	107.8	0.41	3.830E-08	107.6	0.54	3.799E-08	1.0019	1.0082	108.00	3.832E-08
1.5	67.0	0.00	2.386E-08	66.0	0.00	2.365E-08	*1.0152*	1.0089	66.69	2.386E-08

Large Aperture	Brighter Side			Darker Side						
		StDev			StDev		Brighter/Darker		Averages scaled to	
nd	DN	(DN)	Si(amps)	DN	(DN)	Si(amps)	Dn	Si	bright side of mirror	
0	*4019.0*	*0.00*	4.370E-06	*4017.7*	*0.52*	4.331E-06	*1.0003*	1.0090	-	-
0.3	3495.0	1.10	2.304E-06	3473.2	1.64	2.284E-06	1.0063	1.0088	3493.85	2.304E-06
0.5	2102.8	1.10	1.401E-06	2090.7	0.82	1.389E-06	1.0058	1.0086	2102.62	1.401E-06
0.8	1125.2	0.45	7.401E-07	1120.7	3.39	7.337E-07	1.0040	1.0087	1126.10	7.402E-07
1	736.0	0.71	4.864E-07	731.5	0.55	4.826E-07	1.0062	1.0079	735.80	4.867E-07
1.3	393.8	0.45	2.563E-07	391.5	0.55	2.543E-07	1.0059	1.0079	393.75	2.565E-07
1.5	235.0	0.00	1.541E-07	233.7	0.52	1.529E-07	1.0056	1.0078	235.01	1.542E-07
2	146.0	0.00	9.533E-08	145.0	0.00	9.455E-08	1.0069	1.0082	145.91	9.537E-08
2.3	81.8	0.45	5.227E-08	81.7	0.52	5.180E-08	1.0012	1.0091	**81.98**	**5.227E-08**
2.5	51.7	0.52	3.222E-08	51.0	0.00	3.194E-08	*1.0137*	1.0088	**51.49**	**3.222E-08**
						Average Bright/ Dark=	1.0056	1.0088	**2.5 =Bias (from last two points of Large Ap)**	

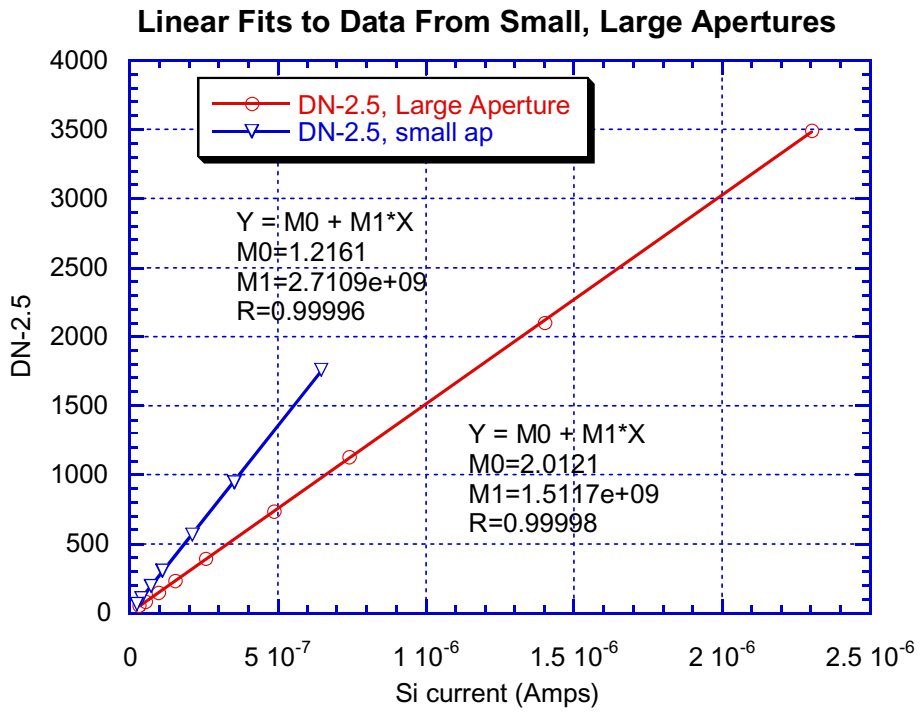

Fig. 2 Observed DN-2.5 plotted versus signal current from the reference standard detector, as labeled, for observations using the two different apertures.

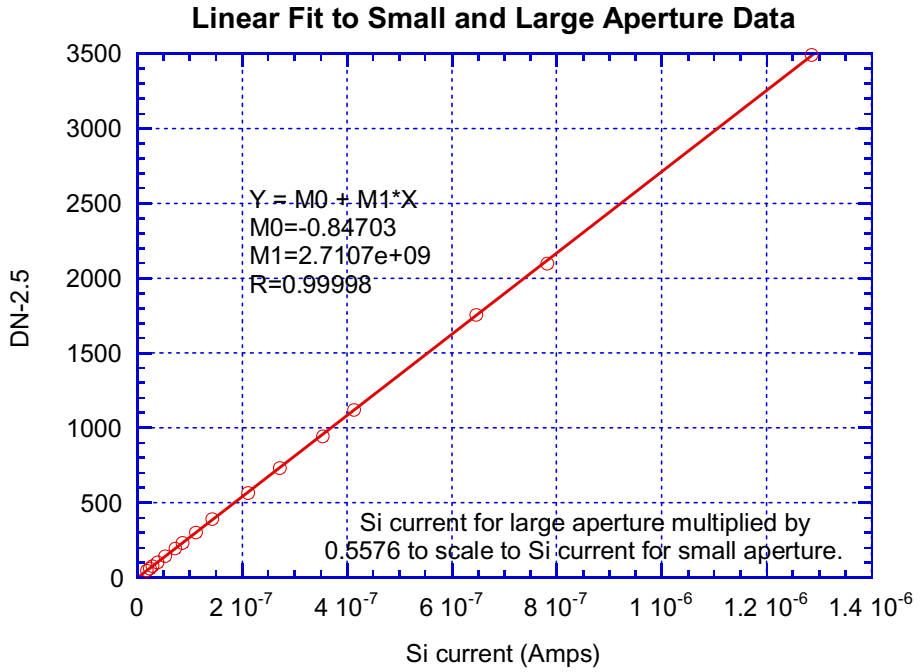

Fig. 3 The observed DN-2.5 is plotted versus the scaled detector current for the large aperture and the unscaled detector current for the small aperture. The slope and intercept of the best least squares line is also shown.

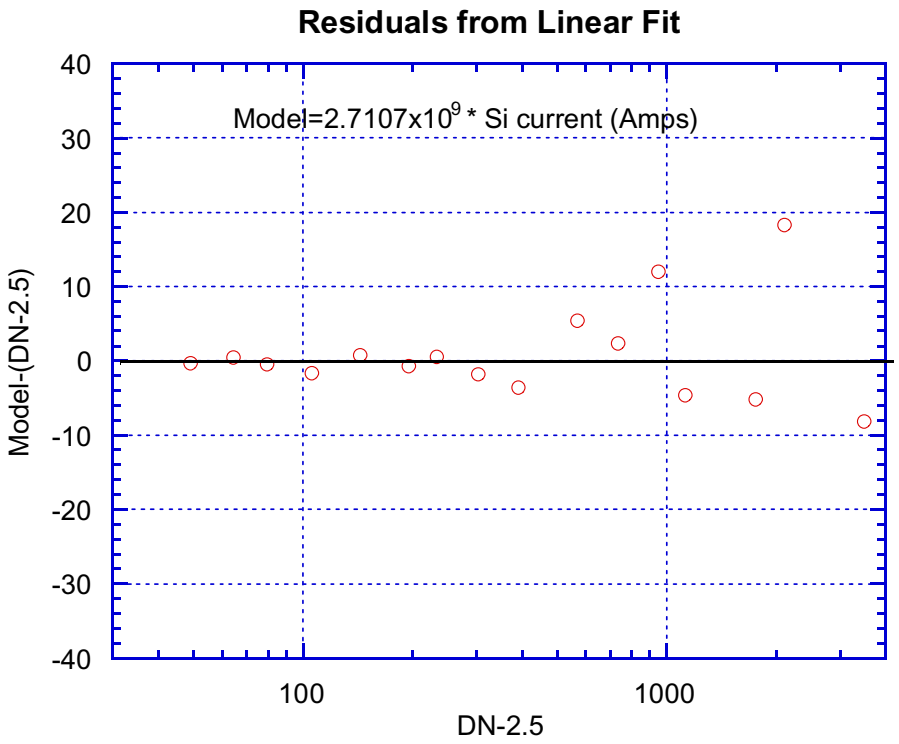

Fig. 4 The linear residuals from a linear fit where DN-2.5 = 2.7107 x 109 times the scaled signal current in amps are shown versus DN-2.5. The residuals seem balanced around zero and increase as the signal from the sun sensor increases.

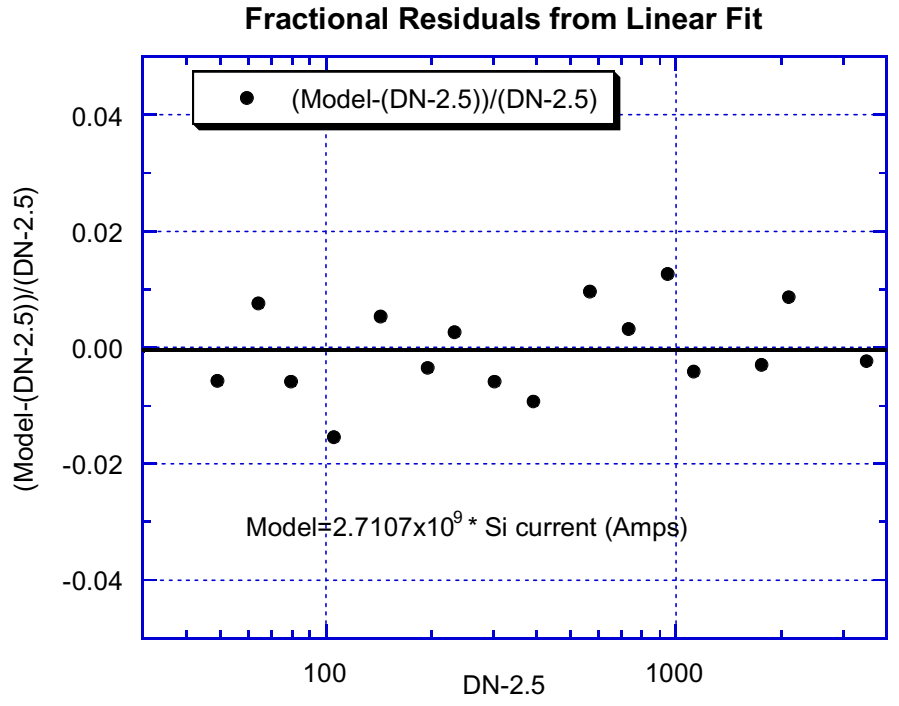

Fig. 5 The fractional residual from the linear fit is shown versus sun sensor signal minus the bias. The fractional residuals are relatively constant at about the 1% level throughout the dynamic range of the sun sensor.

3.0 Absolute Calibration of Sun Sensor at 4 rpm, 50 degrees Solar Zenith Angle

The observations in the Table 1 are sufficient to provide an absolute calibration of the sun sensor if the responsivity of the silicon reference detector are given along with the transmission of the filter over this detector. In addition, the angular field of view of the slits of the sun sensor is needed to evaluate the fraction of the incident flux that will pass through the sun sensor optical system for sources of different angular size.

First, the output of the reference detector can be used to determine the specific flux at the center of the bandpass of the sun sensor. The output of the reference detector, Out, (in Amps) is given by

$$\text{Out (Amps)} = R(943nm)\,F(943nm)\,\Delta A \int \frac{F(\lambda)}{F(943nm)}\,R_{rel}(\lambda)\,T(\lambda)\,d\lambda\,. \qquad (1.)$$

Here the responsivity R of the reference detector at the wavelength of the sun sensor (943 nm) is 0.5082 Amps/Watt, F is the flux of the collimated beam incident on the sun sensor, and the area, ΔA, of the mask over the reference detector is 0.006387 m^2. The relative spectral response of the reference detector, $R_{rel}(\lambda)$, the relative flux of the lamp, and the transmission of the filter over the reference detector, $T(\lambda)$, are given in Table 2. Solving equation (1.) for the flux of the collimated beam gives

$$F(943nm) = \frac{Out(Amps)}{R(943nm)\Delta A \int \frac{F(\lambda)}{F(943nm)} R_{rel}(\lambda)T(\lambda)d\lambda}\,. \qquad (2.)$$

The integral of the product of relative lamp flux, relative spectral response and filter transmission from Table 2 is 6.387 nm. Substitution into equation (2.) for the brightest point from the small aperture (where the reference detector output is 6.4587 x 10^{-7} amps gives the flux incident on the sun sensor as 4.5026 watts/sq.m-micron. Now the responsivity,R*, of the sun sensor at 4 rpm and 50 degrees solar zenith angle is obtained from

$$(1758.25 - 2.5)\ \text{DN} = R^*(\text{DN sq.m micron/Watt})\ E_{smal\ ap}\ \ 4.5026\ \text{Watt/sq.m-micron.} \qquad (3.)$$

Here $E_{smal\ ap}$ is the fraction of the flux from the small aperture that passes through the slits of the sun sensor. Equation (3.) gives

$$R^* = (389.9\ \text{DN/Watt/sq.m})/\ E_{smal\ ap}. \qquad (4.)$$

Using this result, the flux from the direct solar beam at 4 rpm and 50 degrees solar zenith angle can be obtained from the observed sun sensor data number (DN) during Titan entry as

$$\text{Flux(Watts/sq.m-micron)} = ((\text{DN}-2.5)/389.9)\,(E_{\text{small ap}}/E_{\text{sun at Titan}}). \qquad (5.)$$

Here $E_{\text{sun at Titan}}$ is the fraction of the flux of the sun at Titan that makes it through the slits of the sun sensor.

Table 2
Reference Detector, Lamp, and Filter Transmission Variations with Wavelength

Wavelength (nm)	Ref. Detector Responsivity (A/Watt)	Relative Spectral Response	Relative Lamp Flux	Filter Transmis-sion	Rel. Resp* Rel. Lamp* Filter Trans.
930	0.5019	0.9876	1.0281	0.0000	0.0000
931	0.5024	0.9886	1.0258	0.0006	0.0006
932	0.5029	0.9896	1.0235	0.0014	0.0015
933	0.5034	0.9906	1.0212	0.0026	0.0026
934	0.5039	0.9916	1.0189	0.0043	0.0043
935	0.5044	0.9926	1.0165	0.0070	0.0071
936	0.5049	0.9936	1.0141	0.0107	0.0108
937	0.5054	0.9945	1.0117	0.0146	0.0147
938	0.5059	0.9955	1.0094	0.0190	0.0191
939	0.5064	0.9965	1.0071	0.0246	0.0247
940	0.5068	0.9974	1.0049	0.0360	0.0361
941	0.5073	0.9983	1.0031	0.0600	0.0601
942	0.5077	0.9991	1.0015	0.1000	0.1001
943	0.5082	1.0000	1.0000	0.1500	0.1500
944	0.5086	1.0008	0.9985	0.2700	0.2698
945	0.5090	1.0017	0.9969	0.4200	0.4194
946	0.5094	1.0025	0.9954	0.5900	0.5887
947	0.5098	1.0032	0.9938	0.6080	0.6062
948	0.5102	1.0040	0.9923	0.6000	0.5977
949	0.5106	1.0047	0.9906	0.5730	0.5703
950	0.5109	1.0054	0.9890	0.5510	0.5479
951	0.5112	1.0060	0.9873	0.5320	0.5284
952	0.5115	1.0066	0.9856	0.5110	0.5070
953	0.5118	1.0072	0.9839	0.4510	0.4469
954	0.5121	1.0077	0.9821	0.3420	0.3385
955	0.5124	1.0082	0.9804	0.2170	0.2145
956	0.5126	1.0087	0.9786	0.1270	0.1254
957	0.5128	1.0092	0.9769	0.0830	0.0818
958	0.5131	1.0096	0.9751	0.0430	0.0423
959	0.5133	1.0101	0.9733	0.0340	0.0334
960	0.5135	1.0104	0.9716	0.0200	0.0196
961	0.5137	1.0108	0.9698	0.0130	0.0127

962	0.5139	1.0112	0.9680	0.0050	0.0049
963	0.5141	1.0116	0.9662	0.0000	0.0000

We now turn out attention to evaluating the fraction of the incident flux that makes it through the sun sensor slits as a function of the angular size and shape of the source. The power on the sun sensor detector will be the integral over the width of the slits of the convolution of the point spread function of the sun sensor optical system with the angular size of the source. The point spread function of the sun sensor optics was computed using a ray tracing program during the design of the sun sensor. The point spread function from the DISR design review package is shown in Fig. 6 along with a double gaussian approximation to the point spread function. The double gaussian fits the shape of the core of the point spread function, and fits the general level of the wings, although it does not reproduce the detail of the outer rings of the Airy disk. This lack of fidelity is not especially serious, however, since the point spread function must next be integrated in one direction to give the line spread function—a process that significantly smoothes the structure of the outer rings. The line spread function of the double gaussian approximation to the point spread function of Fig. 6 is shown in Fig. 7. Here the line spread function is normalized so that the integral across the function is unity.

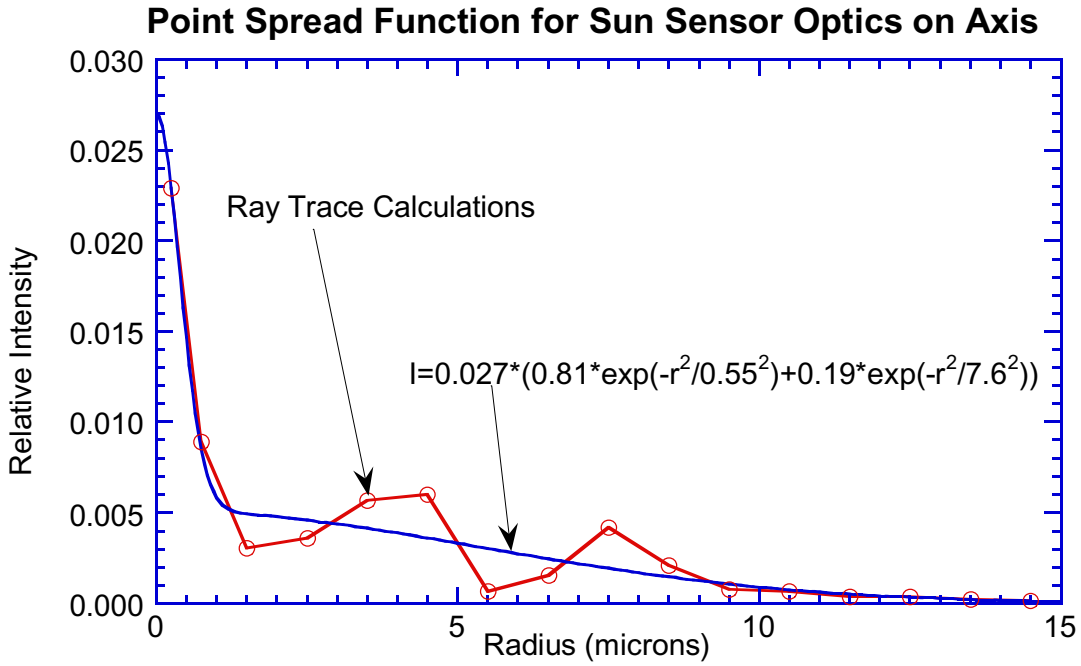

Fig. 6 The point spread function of the sun sensor optics (the same as the Side-Looking Imager optics) as computed by a ray-trace program (points) and as approximated by a double gaussian function (solid line).

Figure 8 shows the convolution of the normalized line spread function with the disk source 0.20 degrees in diameter. The integrated flux in the disk is set to 1 watt/sq.m-micron. The plot shows the integrated energy in slits of width 0.20, 0.25, and 0.30

degrees for various locations of the slits across the source. Thus, the plot shows that the maximum efficiency of the sun sensor optical system for a source 0.2 degrees in diameter is 0.854, 0.934, or 0.974 for slits depending on the width of the slits. The drawing for the reticle specifies the width of the slits as 25 –0, +5 microns. The scale of the sun sensor optics converts 23 microns to 0.20 degrees, as for the side looking imager. Thus the expected slit width is between 0.22 and 0.26 degrees. The observations with the two different sized apertures can be used to determine the width of the slits somewhat more precisely.

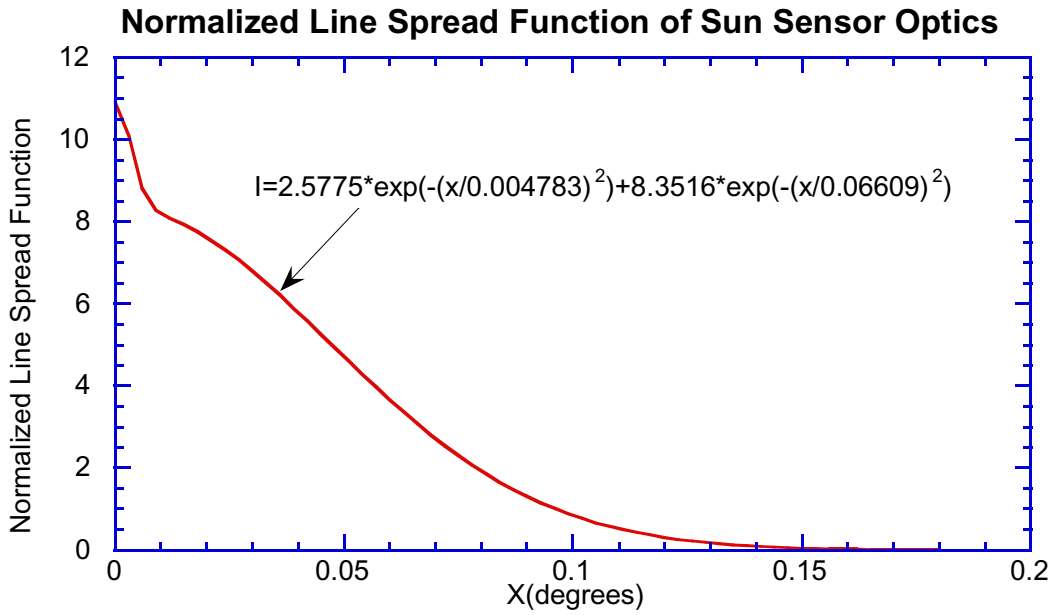

Fig. 7 The normalized line spread function of the sun sensor optics obtained by integration across the point spread function of Fig. 6.

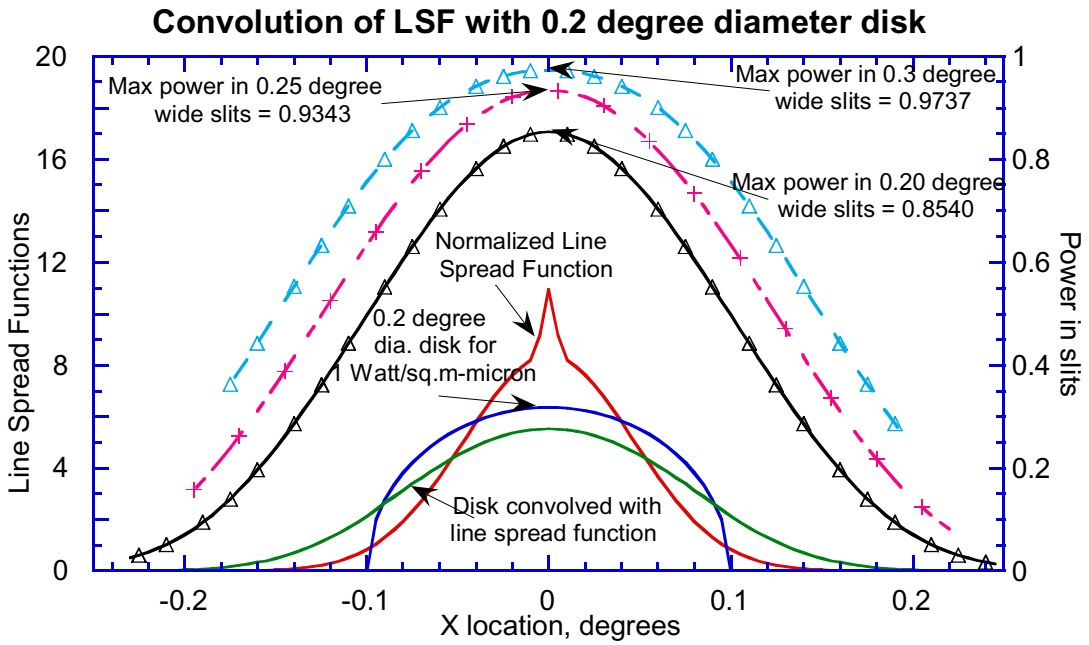

Fig. 8 The normalized line spread function, the variation of the brightness of the 0.2 degree diameter source in one dimension (normalized to an integrated power of 1 watt/sq.m-micron), and the convolution of these two functions. The top three curves show the power on the sun sensor detector by integrating the energy in slits of width 0.2, 0.25 and 0.3 degrees for different locations of the source in the slits. The maximum power in the slits is 0.8540, 0.9343, and 0.9737 for slits for these three widths.

The results of the convolution of the 0.6 inch square aperture with the optical line spread function is shown in Fig. 9. The efficiencies of the square aperture are 0.4166, 0.5203, and 0.6237 for slit widths of 0.20, 0.25, or 0.30 degrees, respectively.

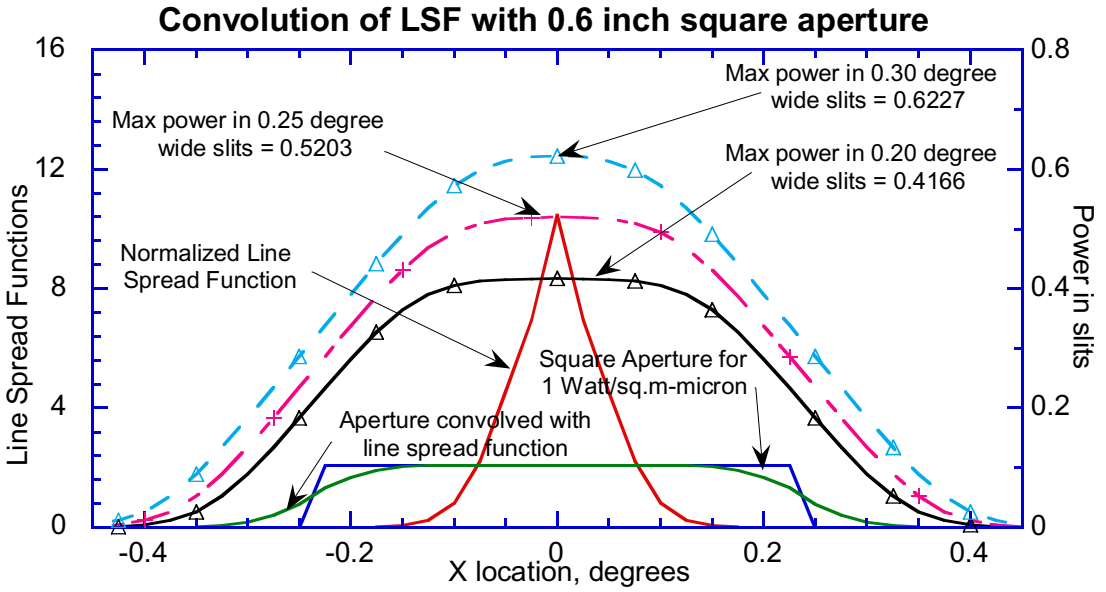

Fig. 9 **Convolution of the normalized line spread function with a square aperture 0.6 inches on each side having an integrated flux of 1 watt/sq.m-micron. The power in slits of width 0.20, 0.25, and 0.30 degrees is shown by the three top curves with the scale on the right. The maximum power in the three slits is 0.4166, 0.5203, and 0.6227 watts/sq.m, respectively, as shown.**

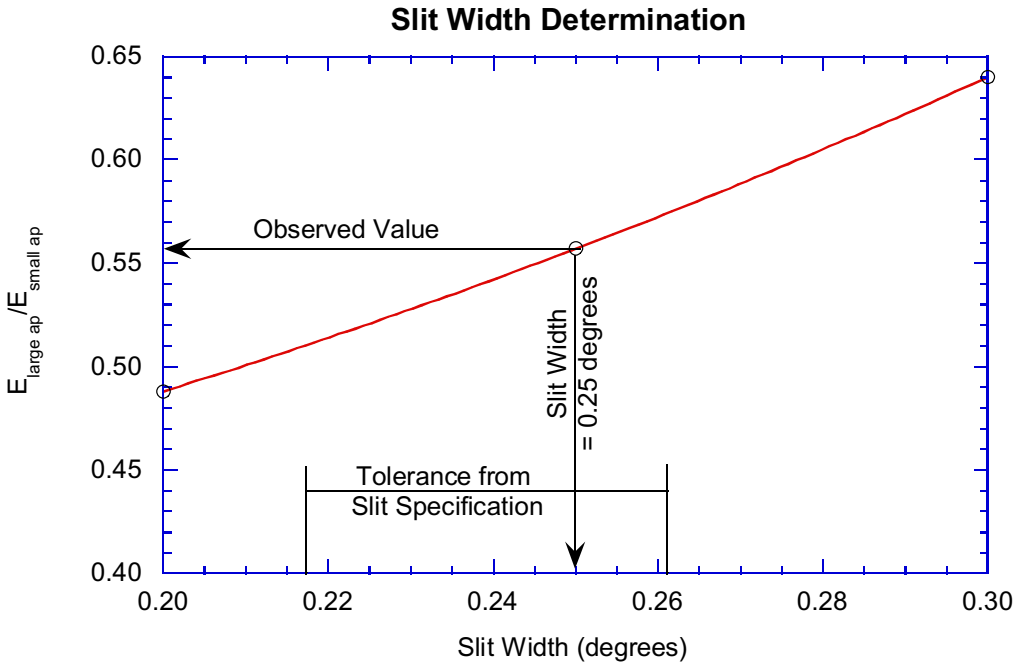

Fig. 10 **The value computed for E large ap/E small ap as a function of slit width is shown. The observed value of 0.5576 implies a slit width of 0.25 degrees, well within the tolerance on slit width specified on the slit drawing.**

Thus, the ratios of the power on the sun sensor detector in the large aperture to the power on the detector for the small aperture are 0.488, 0.557, and 0.640 for slit widths of 0.20, 0.25, and 0.30 degrees, respectively. These values can be compared to the ratio of counts in the observations of the large and small apertures for the same silicon reference detector signal in Fig. 10. This ratio from the observations in Table 1 is 0.5576, in good agreement with the value computed for a slit angular width of 0.25 degrees, or a linear width of 28.75 microns. This width is well within the tolerance given for the reticle drawing. Figure 11 shows that the efficiency factors for the two apertures are able to scale the data numbers minus the bias to the same linear curve for the observations in Table 1.

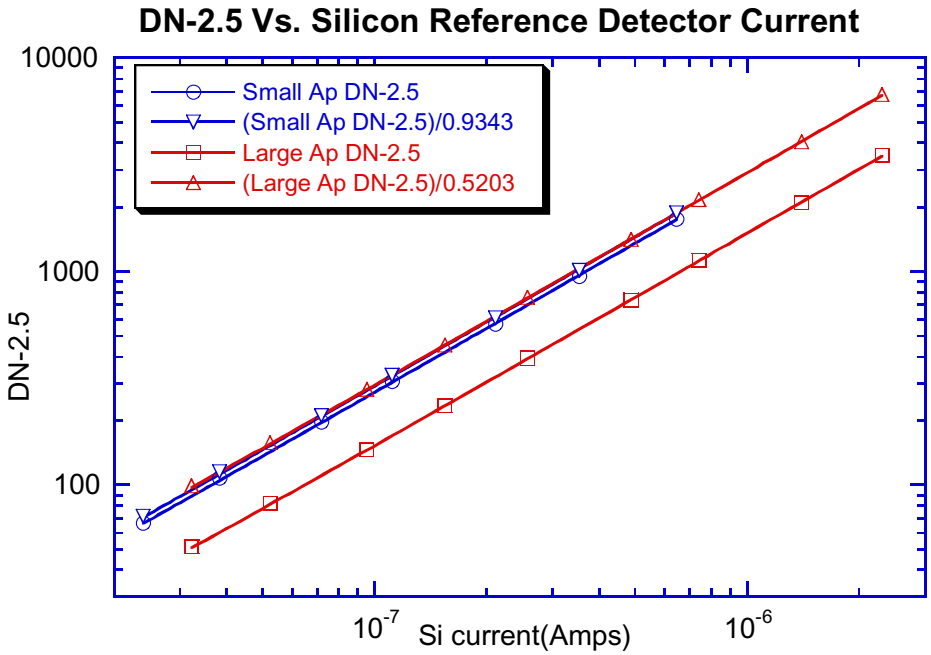

Fig. 11 Small and large aperture DN-2.5 raw and divided by efficiency factors for 0.25 degree wide slits Vs. Silicon Reference Detector Current (Amps). Note that correcting the observations for the different efficiencies of the two apertures puts the data numbers observed for the large and small apertures in good agreement.

Once a good determination of the width of the slits is obtained, a convolution of the normalized line spread function with the size of the sun as seen from Titan can be made to compute the efficiency of the sun sensor system for viewing the sun during the descent. Figure 12 shows the results of the convolution for the sun as seen from Titan. We see that for a slit width of 0.25 degrees, the efficiency for viewing the sun is 0.993.

Accumulating the results for these convolutions, we see that the efficiency with the small round aperture is 0.9343, while the efficiency for viewing the sun at Titan is 0.9931. Thus the flux from the sun can be obtained from the observations at Titan (for 4 rpm spin rate and 50 degrees solar zenith angle) from equation (5.) as

$$\text{Flux}(943\text{ nm}) = (\text{DN-2.5})/\ (414.4\ \text{DN/Watt/sq.m-micron}). \qquad (6.)$$

For completeness, we include Fig. 13 showing the situation for viewing the sun from the Earth. The figure indicates that some 56.3% of the flux from the sun will reach the sun sensor detector for slits 0.25 degrees wide. This is in good agreement with the measurements made using the field test unit (SN02) from the roof of our laboratory in Tucson.

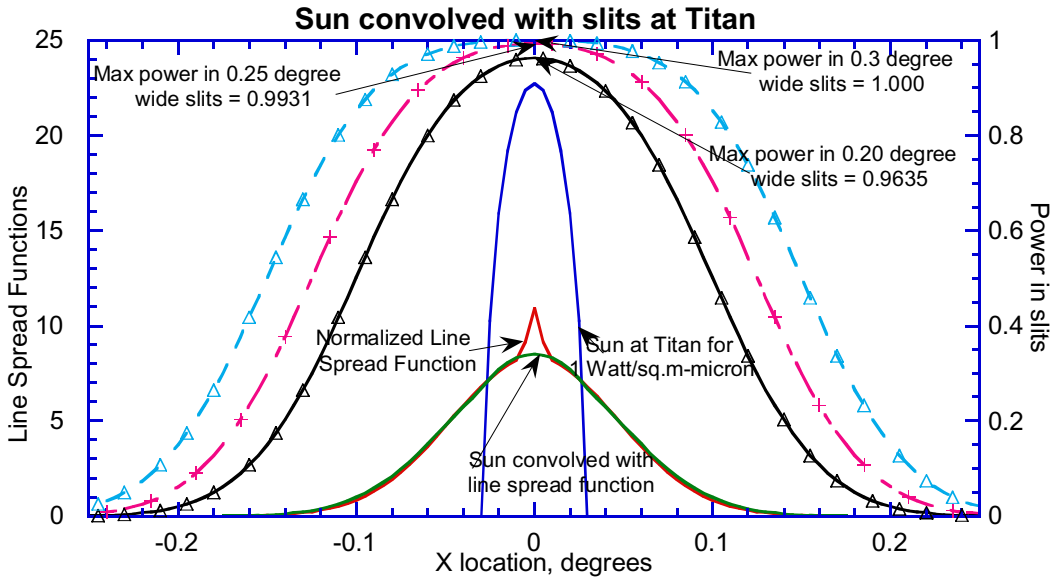

Fig. 12 The line spread function convolved with the size of the sun as seen from Titan is shown on the scale on the left. The right scale shows the power in the slits as a function of slit width and position for slits of width 0.20, 0.25, and 0.30 degrees, as labeled. A slit width of 0.25 degrees implies that the sun sensor system will pass some 99.3% of the energy from the sun at Titan to the sun sensor detector.

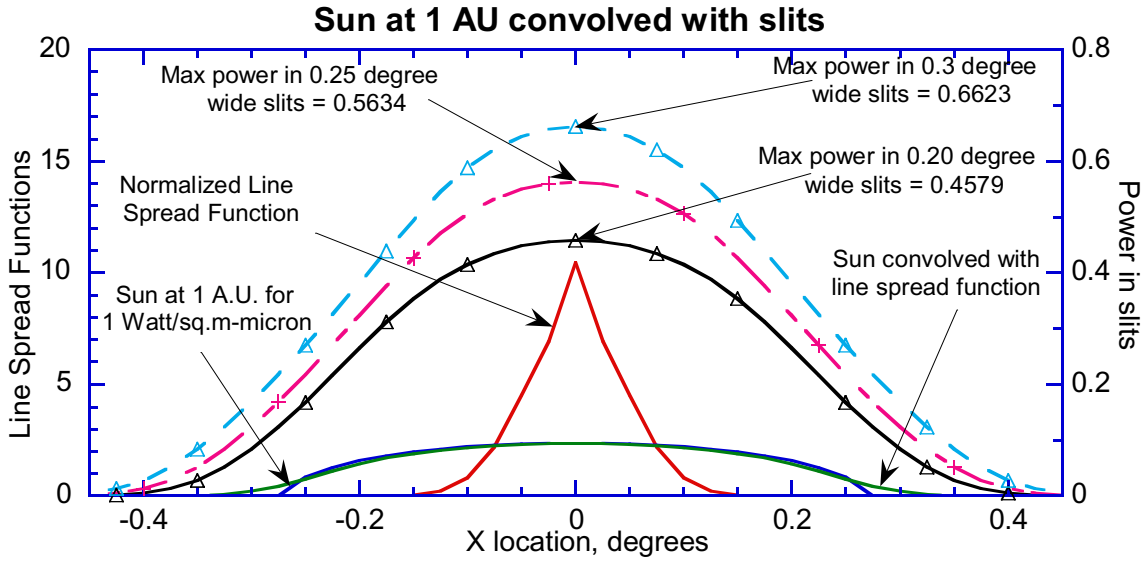

Fig. 13 The convolution of the normalized line spread function with the solar disk as seen from the Earth (along the left scale). The power in the slits of various widths and locations across the disk of the sun is shown on the right scale. Note that for slits 0.25 degrees wide a maximum of some 56.3% of the flux from the sun is registered on the sun sensor detector.

4.0 Variation in Responsivity with Elevation Angle

On September 4, 1996, the we used the rotating mirror mechanism with the collimator to stimulate the sun sensor at 20 rpm and at 4 rpm. The SN03 sensor head was mounted on the altitude-azimuth mount in front of the collimator such that the elevation angle from the baseplate of the sensor head to the direction of incident collimated illumination could be adjusted over the field of view of the sun sensor. Data were collected at elevation angles from 13 to 65 degrees. The observations from the brighter and darker sides of the flat mirror at each elevation angle for both rotation rates are shown in Table 3. Here el is the elevation angle of the observations, DN are the raw averaged data numbers, sigma pop is the standard deviation of the raw data numbers for the observation, and n is the number of samples averaged.

The average ratio of the signal minus the 2.5 DN bias of the flat mirrors on the two sides of the rotating flat plate is 1.0044 for these observations. The observations minus the bias for the darker side were multiplied by this ratio and averaged with the corresponding measurements for the brighter mirror. The readings at 20 rpm and at 4 rpm were divided by the reading at 40 degrees elevation angle to give the column labeled Relative Reading at each rotation rate. The relative readings at 4 rpm were divided by the relative readings at 20 rpm at each elevation angle, and the average ratio of the readings for the two rotation rates was determined to be 0.9911. The relative readings at 4 rpm were divided by this factor to scale them to the equivalent measurements at 20 rpm, and the results for both rotation rates were averaged to give the results in Table 4.

The relative variation in response with elevation angle in Table 4 can be fit reasonably well by a polynomial in elevation angle. The result of rescaling the relative response so the polynomial gives 1.00 for the relative response at 40 degrees elevation angle is shown by the third column in Table 4, while the polynomial fit is in the fourth column and the residuals are in the last column.

Table 3
Observations to Measure Relative Response with Elevation Angle

	Brighter side			Darker side					
	rpm=20							Average DN-2.5 scaled to	
el	DN	sigma pop	n	DN	sigma pop	n	(Bright-2.5) /(Dark-2.5)	brighter side	Relative Reading
13	845.8	1.58	20	844.8	1.54	20	1.0012	844.65	0.5233
15	1028.0	2.25	16	1026.9	3.73	15	1.0011	1027.19	0.6364
20	1220.2	3.10	12	1217.6	3.59	11	1.0021	1219.06	0.7553

25	1376.1	2.64	12	1371.6	2.80	11	1.0033	1374.35	0.8515	
30	1503.6	4.89	12	1498.3	4.15	11	1.0035	1501.73	0.9304	
35	1606.4	3.18	12	1595.3	3.41	11	1.0070	1601.84	0.9925	
40	1615.9	3.31	8	1610.1	4.70	8	1.0036	1614.02	1.0000	
45	1646.5	3.89	8	1639.6	3.58	8	1.0042	1644.14	1.0187	
50	1610.5	3.82	8	1605.9	3.87	8	1.0029	1609.21	0.9970	
55	1500.9	4.46	8	1499.6	5.34	8	1.0009	1501.03	0.9300	
60	1363.9	4.64	8	1362.1	4.58	8	1.0013	1363.48	0.8448	
65	1199.1	4.22	8	1195.5	4.57	8	1.0030	1197.41	0.7419	
	rpm=4									Rel at 4rpm/ Rel at 20 rpm
15	1058.0	1.87	5	1054.0	2.45	5	1.0038	1055.80	0.6259	0.9834
20	1259.5	1.29	4	1254.5	3.42	4	1.0040	1257.24	0.7453	0.9867
25	1425.3	4.65	4	1414.3	2.63	4	1.0078	1420.39	0.8420	0.9888
30	1561.0	3.56	4	1551.5	4.51	4	1.0061	1557.14	0.9230	0.9921
35	1670.3	3.78	4	1654.3	7.50	4	1.0097	1663.42	0.9860	0.9935
40	1693.8	3.20	4	1677.8	5.91	4	1.0096	1686.97	1.0000	1.0000
45	1716.0	5.48	4	1705.0	2.71	4	1.0065	1711.73	1.0147	0.9961
50	1674.0	1.41	4	1665.5	6.35	4	1.0051	1670.89	0.9905	0.9934
55	1557.3	2.06	4	1549.0	3.65	4	1.0054	1554.04	0.9212	0.9905
60	1408.0								0.8332	0.9862
						B/D=	1.0044			
									relative at 4 rpm /relative at 20 rpm=	0.9911

Figure 14 shows the rescaled relative response as a function of elevation angle together with the polynomial fit. The equation for the cubic fit is

$$DN'(40\ degeees) = DN'(elevation) / (0.024329+0.046798*el-5.7087x10^{-4}*el^2+2.6784x10^{-7}*el^3). \quad (7.)$$

Here DN' represents the data number minus the bias of 2.5, and el is the elevation angle in degrees. The residuals from the polynomial fit are shown in Fig. 15.

Table 4
Relative Response vs. Elevation Angle

Elevation Angle (degrees)	Relative Response	Scaled Relative Response	Model Relative Response	Model - Observed
13	0.5233	0.5147	0.5368	0.0221
15	0.6340	0.6235	0.5987	-0.0247
20	0.7536	0.7412	0.7341	-0.0071
25	0.8505	0.8365	0.8417	0.0052
30	0.9309	0.9155	0.9217	0.0062
35	0.9937	0.9773	0.9744	-0.0028
40	1.0045	0.9879	1.0000	0.0121
45	1.0212	1.0044	0.9986	-0.0057
50	0.9982	0.9817	0.9705	-0.0112

55	0.9297	0.9144	0.9159	0.0015
60	0.8427	0.8288	0.8350	0.0062
65	0.7419	0.7296	0.7279	-0.0017

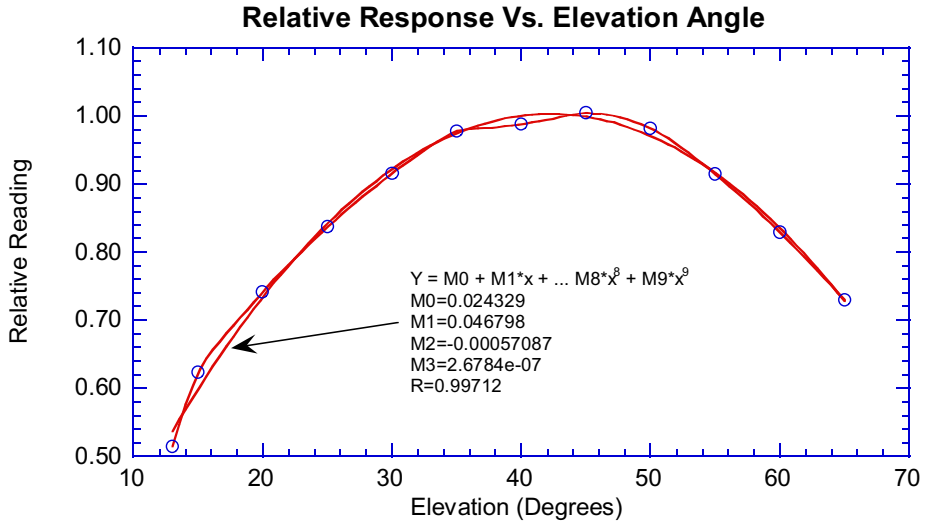

Fig. 14 The relative response of the sun sensor (data number minus bias) as a function of elevation angle is shown. A third order polynomial fit is also shown that has a relative response of 1.00 at 40 degrees elevation.

The observations at 4 rpm and at 20 rpm both showed the same sense of the deviations from the polynomial fit between 35 and 50 degrees elevation, so some of the structure seen in the residuals is probably due to real variations in the width of the sun sensor slits along their length instead of random noise in the measurements. However, since the measurements were only made every 5 degrees in elevation, the structure was badly undersampled. Hence, the polynomial fit is likely to be about as good as a more complex interpolation in the calibration points shown in Fig. 14. In any case, the deviations from the polynomial fit are of the order of 1%, and likely will not be the limiting factor in the quality of the sun sensor measurements of the direct beam flux.

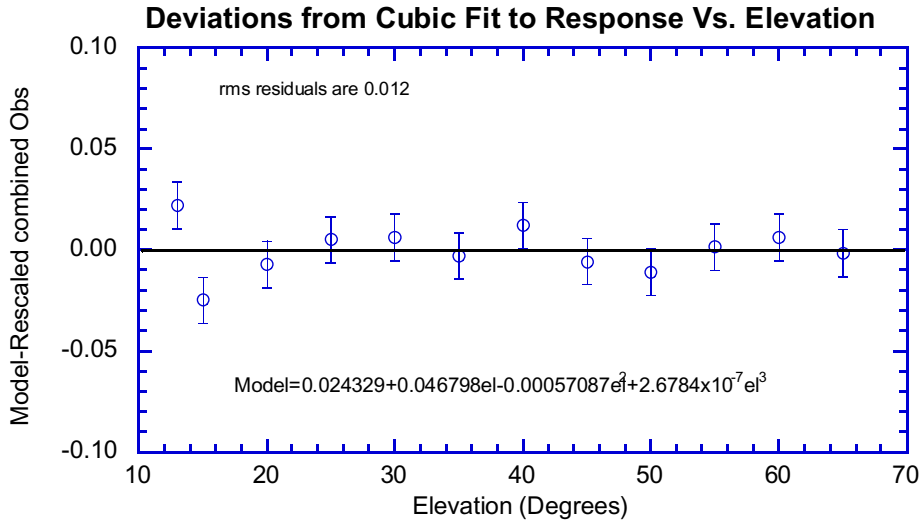

Fig. 15 The residuals to the polynomial fit shown in Fig. 14. The rms residual is about 1%. Nevertheless, some of the structure seen in the residuals is likely to be due to real variations in the width of the sun sensor slits along their length rather than due to random noise.

Thus, in the reduction of the sun sensor observations on Titan, the data numbers minus the bias must be converted to the corresponding values at 40 degrees elevation using equation (7.) before equation (6.) can be used to determine the flux in the direct solar beam.

5.0 Variation in Responsivity with Spin Rate

On September 5, 1996, the sun sensor on the flight model instrument was stimulated at rotation rates between 1 and 25 rpm at three different elevation angles of 17, 40, and 64 degrees. Again, several observations were made from each side of the flat mirror at each rotation rate and elevation angle. The observations are shown in Table 5. Again, we combine the data from both the brighter and darker mirrors by subtracting the bias and scaling the darker observations by the average ratio of the reflectivities of the two mirrors and averaging. The combined observations minus the bias are shown in Table 5.

There is no significant difference in the response as a function of spin rate measured at each of the three elevation angles. To minimize the noise in the observations, we combine the data at all three elevation angles. In Table 6, we find the average ratios of the observations at 17 degrees elevation to the observations at 40 degrees elevation. We average the ratio for the observations at all rotation rates, and rescale the observations to 40 degrees. We do the same for the observations at 64 degrees. The observations at all three elevations are averaged at each rotation rate in Table 6.

Finally, in Table 7, the observations at all rotation rates and scaled to 40 degrees elevation are divided by the average reading at 4 rpm to scale the observations at all elevations and rotation rates to an elevation of 40 degrees and a rotation rate of 4 rpm. These are the data we will try to fit as a function of rotation rate.

Table 5
Sun Sensor Signal Vs. Spin Rate at Three Elevation Angles

El.=17									
	Brighter			Darker			B-2.5/	combined	
rpm	Side	σ	n	Side	σ	n	D-2.5	-2.5	σ
0.99840	1231.8	2.496	4	1223.0	2.082	3	1.0072	1227.22	1.62
1.99690	1232.0	1.958	4	1226.3	0.629	4	1.0047	1228.98	0.91
3.00000	1229.5	0.500	4	1223.3	1.031	4	1.0051	1226.22	0.54
3.99820	1224.7	1.202	7	1217.7	1.190	6	1.0057	1221.03	0.85
4.99660	1229.6	0.972	7	1223.1	1.223	7	1.0053	1226.20	0.78
6.00000	1221.7	1.280	9	1212.9	1.184	9	1.0073	1217.11	0.87
7.00000	1209.2	1.024	9	1205.8	1.854	9	1.0029	1207.32	1.02
7.99648	1208.8	1.077	9	1205.3	0.782	9	1.0029	1206.87	0.66

9.00000	1195.6	1.396	9	1195.2	0.940	9	1.0003	1195.19	0.83
9.99867	1211.2	0.830	9	1209.9	1.020	9	1.0011	1210.38	0.65
10.9977	1212.3	0.667	9	1208.2	0.909	9	1.0034	1210.10	0.56
12.9985	1214.4	1.405	9	1213.2	0.778	9	1.0010	1213.66	0.77
15.0000	1199.0	1.054	9	1190.1	1.241	9	1.0075	1194.34	0.81
16.9986	1209.9	0.824	9	1204.7	1.113	9	1.0043	1207.09	0.68
18.9988	1196.0	1.312	9	1195.9	0.588	9	1.0001	1195.74	0.67
22.9964	1183.0	0.866	9	1180.2	0.940	9	1.0024	1181.38	0.64
24.9979	1168.0	0.957	9	1162.9	1.348	9	1.0044	1165.18	0.81
							1.0039	= ave.	
							0.0024	= σ	
EI = 40							0.0006	= σ ave.	
0.99842	1764.5	2.500	2	1754.0	0.000	2	1.0060	1763.00	1.77
1.99685	1764.0	2.595	6	1748.5	0.847	6	1.0089	1759.99	1.22
3.00000	1761.0	1.915	6	1746.0	1.265	6	1.0086	1757.23	1.12
3.99853	1762.3	1.783	6	1750.8	1.515	6	1.0066	1760.32	1.17
6.00000	1742.3	1.453	6	1727.2	1.537	6	1.0088	1738.41	1.06
6.99815	1718.0	1.290	6	1711.0	1.693	6	1.0041	1718.10	1.05
7.99648	1729.2	1.014	6	1710.2	1.376	6	1.0111	1723.27	0.84
8.99928	1698.0	2.000	2	1685.0	3.000	2	1.0077	1695.01	1.77
9.99767	1729.3	1.116	6	1723.3	2.044	6	1.0035	1729.98	1.12
10.9955	1737.0	1.412	7	1734.3	0.843	6	1.0015	1739.35	0.80
12.9991	1751.5	1.258	6	1737.9	1.335	7	1.0079	1748.38	0.92
15.0000	1716.7	1.063	7	1692.0	2.191	6	1.0146	1707.89	1.15
16.9980	1723.4	1.462	7	1705.3	1.085	6	1.0106	1717.96	0.90
18.9982	1706.3	1.346	8	1697.0	2.007	9	1.0055	1705.18	1.19
22.9964	1662.8	1.631	9	1657.4	0.944	9	1.0032	1663.52	0.91
24.9990	1639.5	1.424	15	1630.3	1.609	15	1.0057	1638.24	1.07
							1.0071	= ave.	
							0.0034	= σ	
EI=64							0.0008	= σ ave.	
2.99990	1335.0	1.000	2	1327.5	1.000	2	1.0057	1332.95	0.71
3.99850	1337.8	0.750	4	1330.7	1.856	3	1.0053	1335.92	0.92
4.99675	1339.4	1.249	5	1329.3	0.558	6	1.0076	1336.07	0.64
6.00006	1327.2	0.654	6	1320.3	1.430	6	1.0052	1325.42	0.74
6.99864	1325.7	1.282	6	1310.2	0.543	6	1.0119	1319.56	0.65
7.99637	1320.3	1.134	6	1309.7	1.145	6	1.0082	1316.64	0.81
9.00050	1307.0	1.095	6	1297.8	1.851	6	1.0071	1304.02	1.04
9.99917	1319.0	0.931	6	1318.0	0.894	6	1.0008	1320.17	0.65
10.9955	1325.2	1.195	6	1321.0	1.366	6	1.0032	1324.76	0.91
12.9991	1329.8	1.302	6	1323.2	1.249	6	1.0050	1328.18	0.90
15.0000	1311.7	1.256	6	1296.0	1.949	6	1.0121	1305.43	1.13
16.9976	1315.3	2.076	6	1302.8	0.601	6	1.0096	1310.70	0.95
18.9982	1305.2	1.108	6	1299.2	0.601	6	1.0046	1303.78	0.60
22.9964	1280.8	1.078	6	1277.3	0.803	6	1.0027	1280.62	0.67
24.9990	1269.2	0.872	6	1261.5	0.719	6	1.0061	1266.82	0.56
							1.0063	= ave.	

							0.0032	= σ	
							0.0008	= σ ave.	

Table 6
Scaling of response Vs. Spin Period to Equivalent Elevation of 40 degrees

						rescaled	rescaled		
rpm	el=17	el=40	el=64	el17/el40	el64/el40	el17	el64	average	sigma
1	1227.2	1763.0		0.6961		1751.9		1757.4	7.86
2	1229.0	1760.0		0.6983		1754.4		1757.2	3.95
3	1226.2	1757.2	1332.9	0.6978	0.7586	1750.5	1743.9	1750.5	6.65
4	1221.0	1760.3	1335.9	0.6936	0.7589	1743.0	1747.8	1750.4	8.92
5	1226.2		1336.1			1750.4	1748.0	1749.2	1.71
6	1217.1	1738.4	1325.4	0.7001	0.7624	1737.4	1734.1	1736.6	2.27
7	1207.3	1718.1	1319.6	0.7027	0.7680	1723.5	1726.4	1722.7	4.22
8	1206.9	1723.3	1316.6	0.7003	0.7640	1722.8	1722.6	1722.9	0.34
9	1195.2	1695.0	1304.0	0.7051	0.7693	1706.2	1706.1	1702.4	6.41
10	1210.4	1730.0	1320.2	0.6997	0.7631	1727.8	1727.2	1728.3	1.45
11	1210.1	1739.3	1324.8	0.6957	0.7616	1727.4	1733.2	1733.3	5.96
13	1213.7	1748.4	1328.2	0.6942	0.7597	1732.5	1737.7	1739.5	8.08
15	1194.3	1707.9	1305.4	0.6993	0.7644	1704.9	1707.9	1706.9	1.71
17	1207.1	1718.0	1310.7	0.7026	0.7629	1723.1	1714.8	1718.6	4.21
19	1195.7	1705.2	1303.8	0.7012	0.7646	1706.9	1705.8	1706.0	0.90
23	1181.4	1663.5	1280.6	0.7102	0.7698	1686.4	1675.5	1675.1	11.46
25	1165.2	1638.2	1266.8	0.7112	0.7733	1663.3	1657.4	1653.0	13.11
				0.7005	0.7643	=ave.			
				0.0051	0.0044	= σ			
				0.0013	0.0012	= σ ave.			

Table 7
Relative Response Scaled to 40 degrees elevation and 4 rpm

	average		el 17	el 40	el 64
	relative	σ of	rel to ave	rel to ave	rel to ave
rpm	to 4 rpm	average	at 4 rpm	at 4 rpm	at 4 rpm
1	1.0040	0.0045	1.0009	1.0072	
2	1.0039	0.0023	1.0023	1.0055	
3	1.0001	0.0038	1.0000	1.0039	0.9963
4	1.0000	0.0051	0.9958	1.0057	0.9985
5	0.9993	0.0010	1.0000		0.9986
6	0.9921	0.0013	0.9926	0.9932	0.9907
7	0.9842	0.0024	0.9846	0.9816	0.9863
8	0.9843	0.0002	0.9843	0.9845	0.9841
9	0.9726	0.0037	0.9747	0.9684	0.9747
10	0.9874	0.0008	0.9871	0.9883	0.9868
11	0.9903	0.0034	0.9869	0.9937	0.9902
13	0.9938	0.0046	0.9898	0.9988	0.9927
15	0.9752	0.0010	0.9740	0.9757	0.9757
17	0.9819	0.0024	0.9844	0.9815	0.9797
19	0.9746	0.0005	0.9752	0.9742	0.9745
23	0.9570	0.0066	0.9635	0.9504	0.9572
25	0.9444	0.0075	0.9503	0.9359	0.9469

The relative response at each elevation angle scaled to the average response at 4 rpm and 40 degrees elevation are shown in Fig. 16. We see that the relationship between relative response and rotation rate seems to have three lobes. This effect is visible in the

observations at all three elevation angles. Unless the curve is fitted separately in the regions slower than 9 rpm, between 9 and 15 rpm, and faster than 15 rpm, simple polynomials in rotation rate have much larger residuals than expected from the quality of the observations. Figure 16 shows a model fitted in this piecewise manner. The relationship is

$$\begin{aligned} &\text{for rpm} < 9, && R = 1.0029+0.0012856*rpm-0.00050206*rpm^2, \\ &\text{for } 9 < \text{rpm} < 15, && R=0.65922+0.055632*rpm-0.00203038*rpm^2, \\ &\text{for rpm} > 15, && R=0.83228+0.017428*rpm-0.00051928*rpm^2. \end{aligned} \qquad (8.)$$

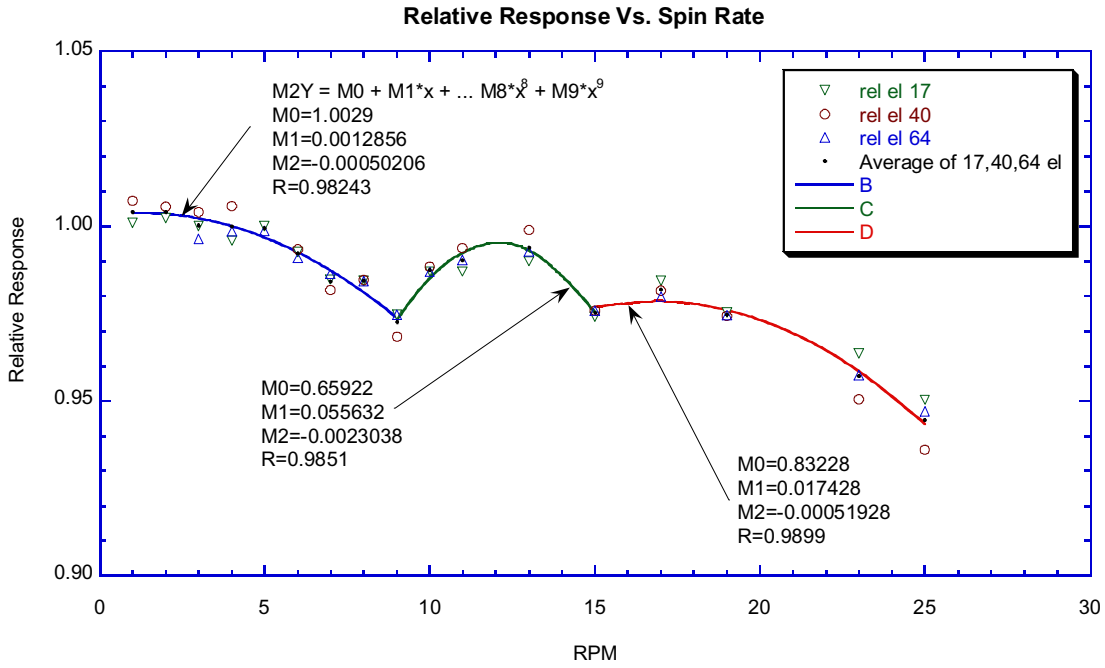

Fig. 16 Relative response of the sun sensor at 17, 40, and 64 degrees elevation scaled to 40 degrees elevation as a function of spin rate, as indicated in the key. The data plotted are from Table 7. The three portions of the curve for rpm<9 rpm, between 9 and 15 rpm, and >15 rpm are fitted by the curves as labeled.

The residuals of the scaled observations to the model are shown in Fig. 17. Note that the residuals are all less than 1%, with the rms residual being 0.35%. The quality of the fit is as good as we have seen for the transfer function, absolute calibration, and relative response as a function of elevation angle. The complex structure likely results from the time constant of the electronics used to suppress noise at fast rotation rates.

Thus, the procedure for converting the data numbers from the sun sensor to the flux in the direct solar beam is as follows. First, the bias of 2.5 DN is subtracted from the observed data number. Then the observations are scaled to their equivalent values at an elevation angle of 40 degrees using equation (7.). The data numbers are corrected to an equivalent spin rate of 4 rpm by dividing by the relative response at the observed rotation rate relative to 4 rpm given by equation (8.). Finally, the corrected data number minus the bias at 40 degrees elevation and 4 rpm is divided by 414.4 DN/(Watt/sq.m-micron) from equation (6.) to give the absolute flux in the solar beam in Watts/sq.m-micron.

6.0 Variation of Responsivity with Temperature

We measured the variation of the response of the sun sensor with temperature on September 13, 1996. In order to be able to cool the sun sensor, we mounted the sensor head in the insulated dry box with the front end of the sensor head mounted inside the 20 inch diameter integrating sphere. The thermal strap from the focal plane was connected to a strap cooled by liquid nitrogen. Liquid nitrogen from a supply dewar was boiled to produce cold nitrogen gas. We fed this cold gas to the dry box in which the sensor head was mounted. We monitored the temperature of the violet photometer, the optical bench, the focal plane, and the gas inside the box of the sensor head for several hours as the sensor head was cooled by nearly 100 C from ambient, and slowly warmed up again.

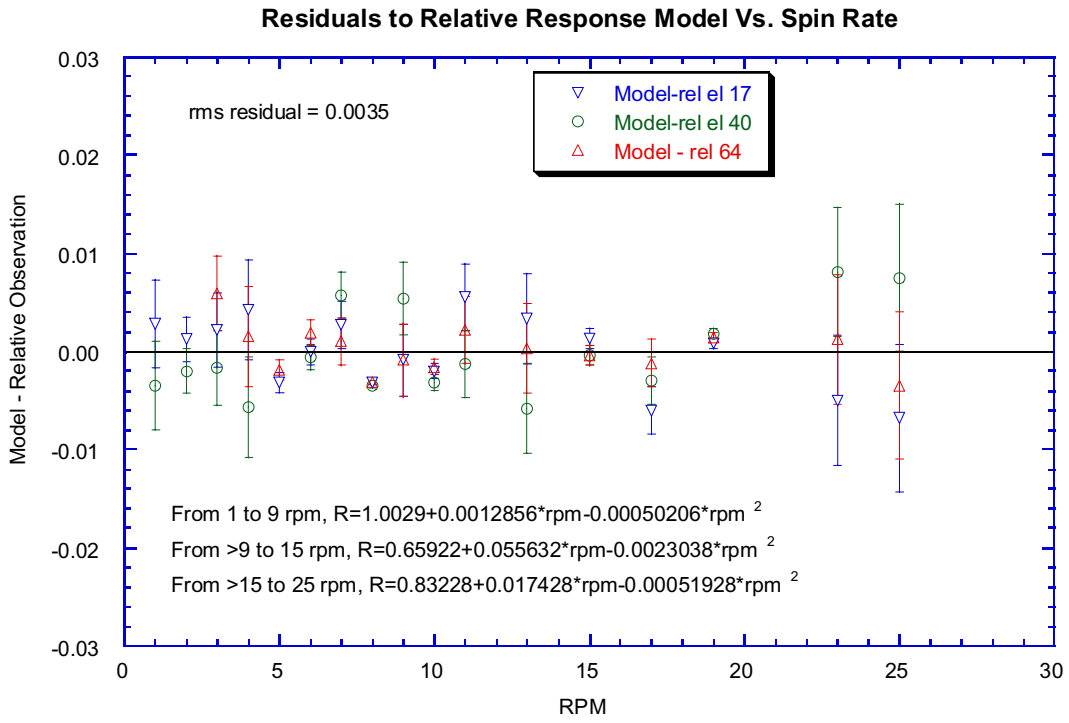

Fig. 17 The residuals from the three-piece model of relative response of the sun sensor are shown as a function of rotation rate for the observations at 17, 40, and 64 degrees elevation, as labeled. The rms residual is 0.35%.

We stimulated the sun sensor with a high intensity lamp positioned just outside one port of the integrating sphere. We mounted a large metal disk so that it could be rotated between the high intensity lamp and the entrance port of the integrating sphere. Three holes were drilled close to one another on the radius of the disk at which the lamp was positioned. When we rotated the disk, three short flashes from the high intensity lamp illuminated the inside of the integrating sphere on every rotation of the disk. These triplets of illumination stimulated the sun sensor electronics to lock onto the flashes.

We mounted the monochrometer at a second port of the integrating sphere with the standard silicon detector mounted behind the monochrometer. During most of the

run, we set the monochrometer to 940 nm and used the standard silicon detector to monitor the brightness of the light inside the integrating sphere. We stopped the rotation of the disk periodically to permit this measurement. The procedure consisted of rotating the disk for several minutes to permit the sun sensor to lock in the triplets of flashes in the sphere and record the sun sensor signal, followed by halting the rotation of the disk to permit measurements of the brightness in the sphere using the monochrometer set to 940 nm followed by the silicon standard detector and a dark reading of the silicon standard detector. When the temperature reached the minimum value, we halted the rotation of the disk and made a complete scan of the monochrometer to measure the spectrum of the light in the integrating sphere. We then repeated the alternation of the rotation of the disk and reference readings at 940 nm during the period when the sensor head was warmed back to ambient temperature.

The measurements of the sun sensor, the rotation rate, the readings of the silicon reference detector at 940 nm, and the temperature recorded for the optical bench in the sensor head are shown as a function of time during the test in Table 8. Here we averaged n readings of the sun sensor while the disk was rotated before stopping the disk and reading the reference detector and its dark at 940 nm. The times, reference detector readings, and optics temperatures have been interpolated to the mean time of the sun sensor readings in each period when the disk was rotated and the sun sensor was locked. The standard deviation of the sun sensor readings in each case was about 0.4 DN, and the algorithm used to correct the readings to 4 rpm (equation 8) fits to about 0.3%. Thus, the random uncertainty in the readings in the next to last column is less than about 0.5%.

Table 8
Sun Sensor Readings vs. Temperature

Mean Time (sec)	<DN>	n	Rpm	Ref-dark	(DN-2.5) at 4 rpm/ (Ref-dark)	Optics Temperature (K)
10085.9899	99.9	7	1.3149	0.9984	97.15	291.57
10439.4494	99.1	18	1.6408	0.9965	96.55	285.34
10748.2487	99.5	13	1.6392	0.9947	97.20	279.13
11042.3271	98.7	13	1.6403	0.9929	96.53	273.94
11520.3602	98.0	7	1.3203	0.9897	96.13	264.83
11753.7968	97.1	14	1.3177	0.9881	95.43	260.93
12013.7251	97.1	14	1.3183	0.9862	95.54	256.44
12487.8534	95.7	18	1.6408	0.9826	94.53	249.19
12739.0524	95.3	19	1.6391	0.9806	94.26	245.74
12993.7814	94.7	19	1.6384	0.9785	93.87	242.75
13248.2677	93.8	19	1.6384	0.9763	93.17	240.10
13502.6083	93.2	19	1.6376	0.9740	92.79	237.54
13757.0719	92.6	19	1.6392	0.9717	92.36	234.87
14011.5851	91.9	19	1.6407	0.9693	91.89	232.54
14266.0817	91.1	19	1.6384	0.9669	91.31	230.38
14617.2733	90.9	19	1.6376	0.9633	91.48	227.82
14920.7425	90.2	10	1.6391	0.9602	91.00	224.59
15196.8719	87.0	10	1.6390	0.9572	87.95	219.85
15473.1874	87.0	10	1.6392	0.9542	88.23	216.19
15749.9813	86.0	10	1.6405	0.9511	87.47	213.35
16088.1861	85.7	19	1.6399	0.9472	87.56	211.63
16391.6875	85.1	10	1.6435	0.9453	87.06	210.68

16667.5083	85.1	10	1.6405	0.9475	86.86	209.33
18471.7305	88.0	19	1.6430	0.9592	88.81	223.34
18775.4074	89.0	10	1.6406	0.9607	89.71	228.04
19051.2657	89.7	10	1.6434	0.9619	90.32	232.15
19327.3866	90.8	10	1.6406	0.9630	91.35	236.14
19603.5583	90.6	10	1.6390	0.9641	91.05	240.02
19915.3047	91.1	18	1.6400	0.9651	91.43	244.32
20215.5396	91.9	10	1.6406	0.9659	92.22	249.41
20453.2184	93.2	19	1.6407	0.9665	93.51	253.02
20757.0188	94.1	10	1.6407	0.9671	94.37	257.10
21032.9321	94.6	10	1.6376	0.9676	94.84	260.45
21484.8382	94.9	18	1.6383	0.9681	95.09	265.38
21785.3971	95.3	10	1.6391	0.9682	95.50	268.66
22065.4779	96.3	12	1.6404	0.9682	96.47	271.58
22347.7093	96.2	10	1.6419	0.9682	96.43	275.32
22623.7029	96.1	10	1.6435	0.9680	96.34	279.48
23046.5651	96.0	12	1.6367	0.9675	96.29	284.71
23328.9539	96.1	10	1.6378	0.9670	96.44	287.71
23605.3888	96.5	10	1.6420	0.9664	96.92	290.50
23880.8904	97.7	10	1.6405	0.9657	98.22	293.24
24160.7137	98.2	12	1.6403	0.9649	98.79	295.84

When the sun sensor readings corrected for bias, rotation rate, and lamp drift are plotted against optics temperature, hysteresis is seen (Fig. 18). It seems that the temperature of the sun sensor lags slightly behind the temperature of the internal optics both on the way down in temperature and while the unit is warmed up. We assume that the true temperature of the sun sensor is half way between the optics temperature reported during cooling and warming at the same sun sensor reading.

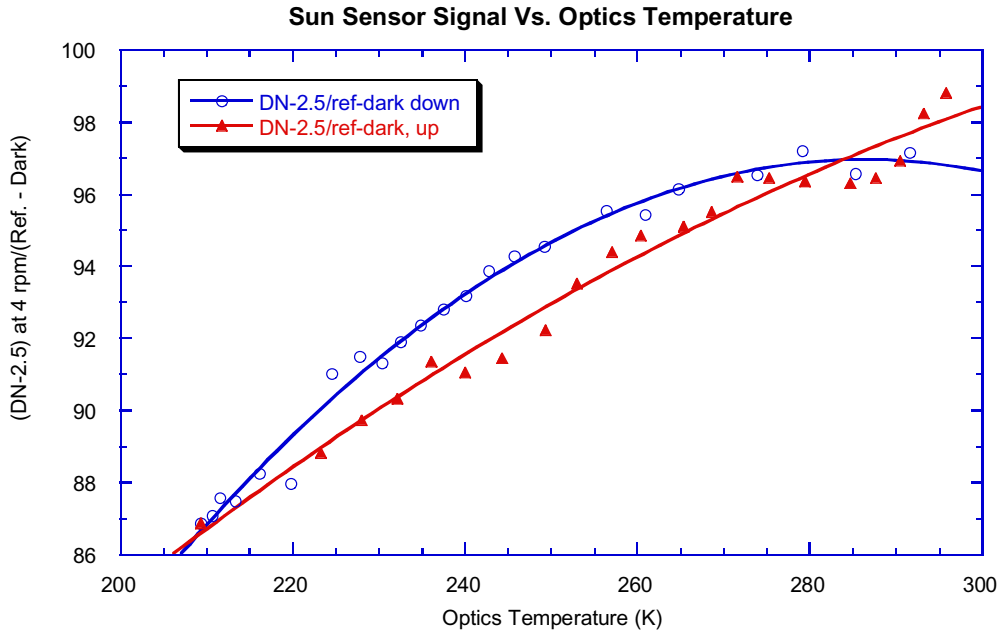

Fig. 18 Sun Sensor signals corrected for bias, rotation rate, and lamp drift are shown plotted against optics temperature. The corrected data numbers are

shown as circles while the temperature is decreasing, and as filled triangles while the temperature is increasing.

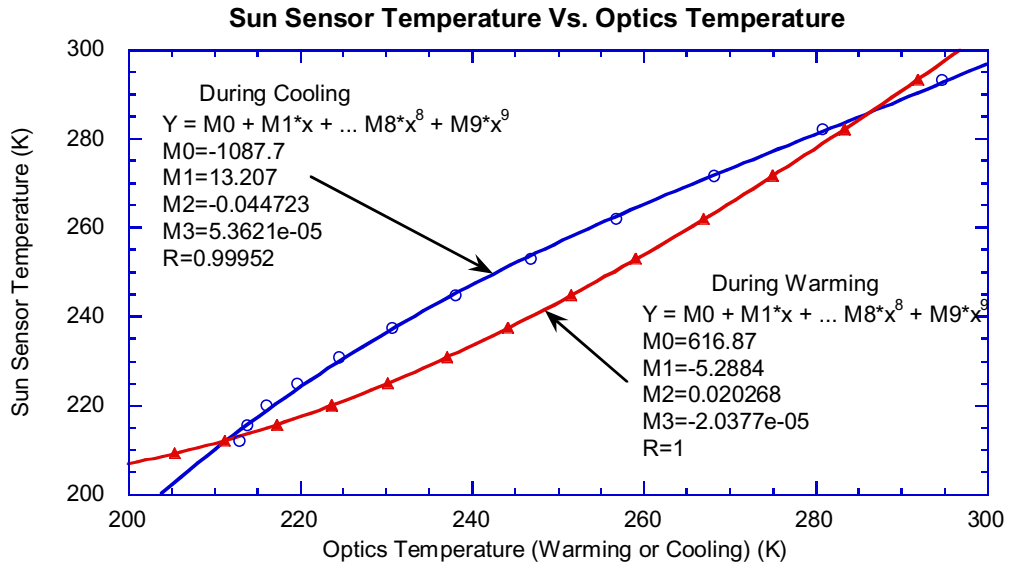

Fig. 19 Average temperature (taken as the best estimate of true sun sensor temperature) versus measured optics temperature during cooling or warming, as labeled. Polynomial fits are shown for correcting the measured optics temperature during cooling or warming to the best estimate for the true sun sensor temperature.

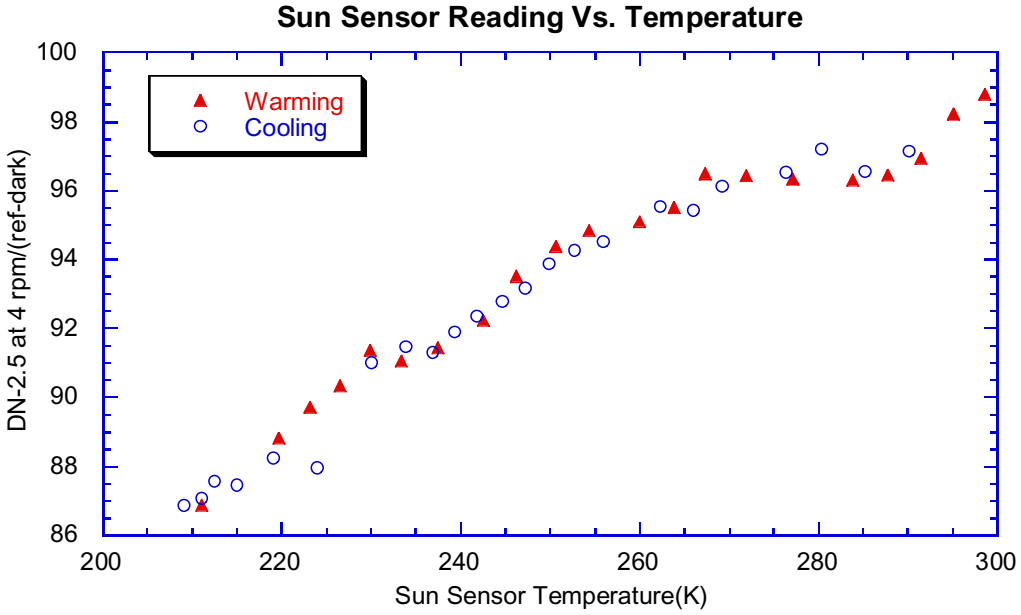

Fig. 20 Corrected sun sensor reading versus best estimate of true sun sensor temperature during cooling or warming. Note that there is now good agreement between the observations during cooling and warming.

Figure 19 shows the average temperature versus the measured optics temperature during cooling and warming. A polynomial fit for each curve is also shown that permits the average temperature on cooling and warming to be obtained from the measured optics temperature in each direction. Figure 20 shows the sun sensor reading at 4 rpm corrected for bias and lamp drift versus the sun sensor temperature. There seems to be no systematic difference now during warming or cooling.

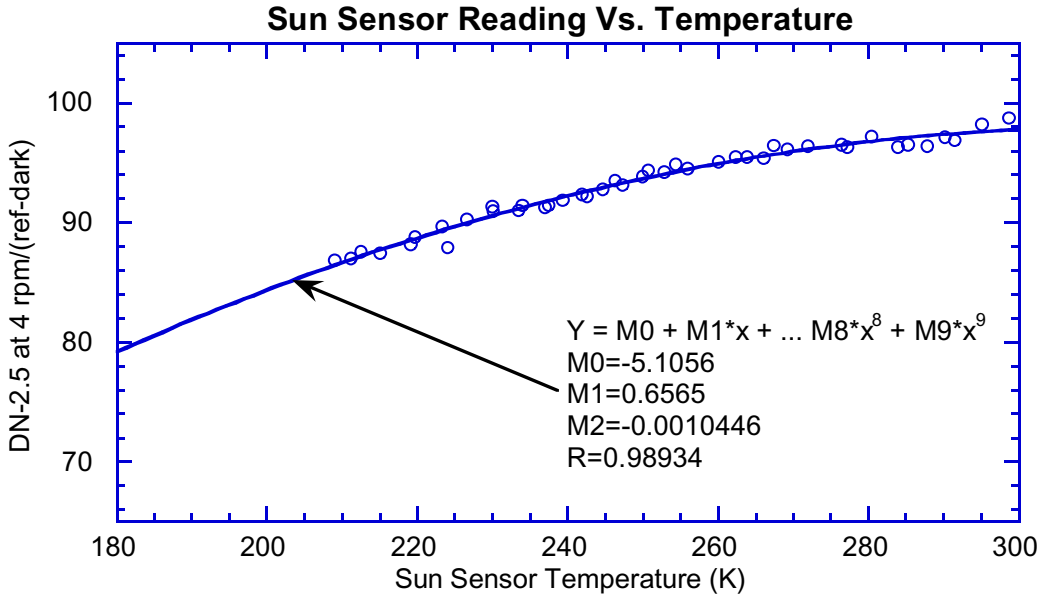

Fig. 21 Sun Sensor reading corrected to 4 rpm and for lamp drift is shown as a function of sun sensor temperature. Coefficients for a second degree polynomial fit are also shown. The temperature of the sun sensor during Titan entry is not expected to get much colder than 200 K.

The optics temperature on September 5, 1996 at the time of the absolute calibration of the sun sensor at 4 rpm using the small aperture was 295.185 K, corresponding to a DN-2.5 = 97.66. The data number at 295.185 K can be obtained from the data number at any other temperature using the polynomial in Fig. 21 normalized to this value. This gives

$$\text{(DN-2.5) at 295.185 K} = \text{(DN-2.5 at T)} / [-0.05228 + 0.006722*T - 1.0696\text{x}10^{-5}*T^2]. \quad (9.)$$

Thus, the absolute flux from the sun sensor at Titan is obtained by subtracting the bias of 2.5 DN, applying equation (7.) to correct the readings to 40 degrees elevation, applying equation (8.) to correct the readings to 4 rpm, applying equation (9.) to correct the readings to 295.185 K, and dividing by 414.4 DN/(Watt/sq.m-micron) to convert to absolute flux.

This prescription works so long as the power on the sun sensor detector is due solely to the flux from the direct solar beam. Some of the signal is also due to the diffuse intensity passing through the slits of the sun sensor. We now estimate the correction required for this effect.

7.0 Responsivity of Sun Sensor to Diffuse Intensity

At the cold temperature, the absolute intensity of the wall of the integrating sphere was measured as a function of wavelength. The measurements are shown in Table 9. At the central wavelength of the sun sensor of 945 nm, the intensity of the wall is 13.11 watts/sq.m-micron-sr. The data number (minus bias) observed at a temperature of 211 K was 87 DN. From equation (9.), this corresponds to 97.8 DN at 295.185 K. Thus the responsivity of the sun sensor for an isotropic diffuse intensity field is 7.46 DN/(Watt/sq.m-micron-sr). Table 10 below shows the direct beam flux and average downward diffuse intensity at several altitudes on Titan from our aggregate particle model. The responsivities used and the data numbers resulting from the direct beam and the diffuse beam are also shown. Note that the signal at 160 km in the nominal model is less than 3500 DN, thus avoiding any potential nonlinearities in the transfer function at large signal levels, at least in the nominal model. The signal estimated from the downward diffuse intensity field is somewhat too low because the diffuse field is larger than average near the sun. This may increase the signal from the diffuse field by a factor of 2 to 5. Even so, it seems that the correction for the contribution of the diffuse intensity to the total sun sensor signal will be only a few percent of the total signal even near the bottom of the atmosphere for our nominal model. In practice, we will have measures of the direct beam from both the upward-looking visible and infrared spectrometers for every ten or so sun sensor measurements. The measurements from these two other DISR instruments can be used to correct the responsivity of the sun sensor for various effects. Even without such a correction, the signals from the sun sensor will give the relative change in extinction optical depth locally with altitude at much higher vertical resolution than would be available from the spectrometer measurements.

Table 9
Absolute Intensity of the Wall of the Integrating Sphere

Wavelength (nm)	Ref. Detector Signal (Amps)	*Responsivity (Amps/ Watt/m^2-micron-sr)	Intensity (Watts/m^2-micron-sr)
900	3.378E-09	1.4541E-10	23.2309
910	3.563E-09	1.8575E-10	19.1817
920	3.802E-09	2.3586E-10	16.1197
930	4.282E-09	3.0449E-10	14.0629
940	5.061E-09	3.8449E-10	13.1629
950	5.959E-09	4.5668E-10	13.0485
960	6.796E-09	5.1171E-10	13.2810
970	7.543E-09	5.5491E-10	13.5932
980	8.190E-09	5.9505E-10	13.7635
990	8.637E-09	6.2993E-10	13.7110
1000	8.820E-09	6.5562E-10	13.4529

*Note: Responsivity is for monochrometer plus reference detector combination.

Table 10
Signal from Direct Beam and Diffuse Intensity Field Vs. Altitude on Titan

Altitude (km)	Direct Beam Watts/sq.m-micron	Diffuse Intensity (Watts/sq.m-micron-sr)	DN from Direct Beam	DN from diffuse intensity
404	9.4012	0.0000	3895.9	0.0
160	8.0540	0.2327	3337.6	1.7
128	6.6072	0.4660	2738.0	3.5
96	4.4181	0.7735	1830.9	5.8
48	2.8183	0.9005	1167.9	6.7
24	2.0658	0.8515	856.1	6.4
0	0.9477	0.5091	392.7	3.8

8.0 Map of Location of Sun Sensor Slits

We determined the locations of the first and third slits relative to the center slit from observations made on September 4, 1996. In this test, the collimated beam was swept past the sensor head in a horizontal plane. The sensor head was mounted on the altitude – azimuth mount facing the collimated beam with the instrument baseplate level. Then the instrument was tipped down so that the collimated beam was in the field of view of the sun sensor. Data were collected throughout a range of tip angles spanning the field of view of the sun sensor. This downward tip angle is the relative elevation angle of the collimated beam in the frame of reference of the sun sensor. The zenith angle of the illumination at the center of the field of view (at the center slit) is 90 minus the relative elevation angle of the illumination.

The data from this test include the times (in tenths of a millisecond) of the crossing of each of the three slits on each rotation of the collimated beam. We can determine the rotation period of the collimated beam from the difference in the times of successive crossings of the center slit. The angular distance between the slits are determined from the difference in time of the slit crossings divided by the period and multiplied by 360 degrees.

These angular distances are not the difference in azimuth angles of the three slits, however, since the rotation of the collimated beam is in the horizontal plane, not about the vertical axis of the sensor head that is tipped toward the beam. We calculate the azimuth differences and the zenith angles at which the first and third slits are observed as follows. Consider two right-handed coordinate systems (see Fig. 22). The unprimed system is in the laboratory frame with Z pointing up and Y pointing toward the collimator when the center slit is illuminated. The primed system is in the frame of the instrument, with Z' pointing upward from the instrument baseplate and the center slit in the Y'-Z'plane. The Z' axis is tipped toward the source by an angle "tip" so that when the collimated beam crosses the center slit the angle of the beam from the Z' axis is the zenith angle ZA. Then the vector pointed toward the beam when it crosses the center slit is

$$Vc = 0\ i' + \cos(tip)\ j' + \sin(tip)\ k'. \qquad (10.)$$

Suppose the first slit is observed earlier in time when the beam is θ_1 degrees before the crossing of the center slit. Then the vector pointing to the source when the first slit is crossed is

$$V_1 = -\sin(\theta_1)\ i' + \cos(\theta_1)\cos(tip)\ j' + \cos(\theta_1)\sin(tip)\ k'. \qquad (11.)$$

Suppose the crossing of the third slit is later in time than the crossing of the center slit corresponding to a rotation θ_2 degrees of the collimated beam past the location of the center slit. Then the vector pointing to the source in the third slit is

$$V_3 = -\sin(\theta_2)\ i' + \cos(\theta_2)\cos(tip)\ j' + \cos(\theta_2)\sin(tip)\ k'. \qquad (12.)$$

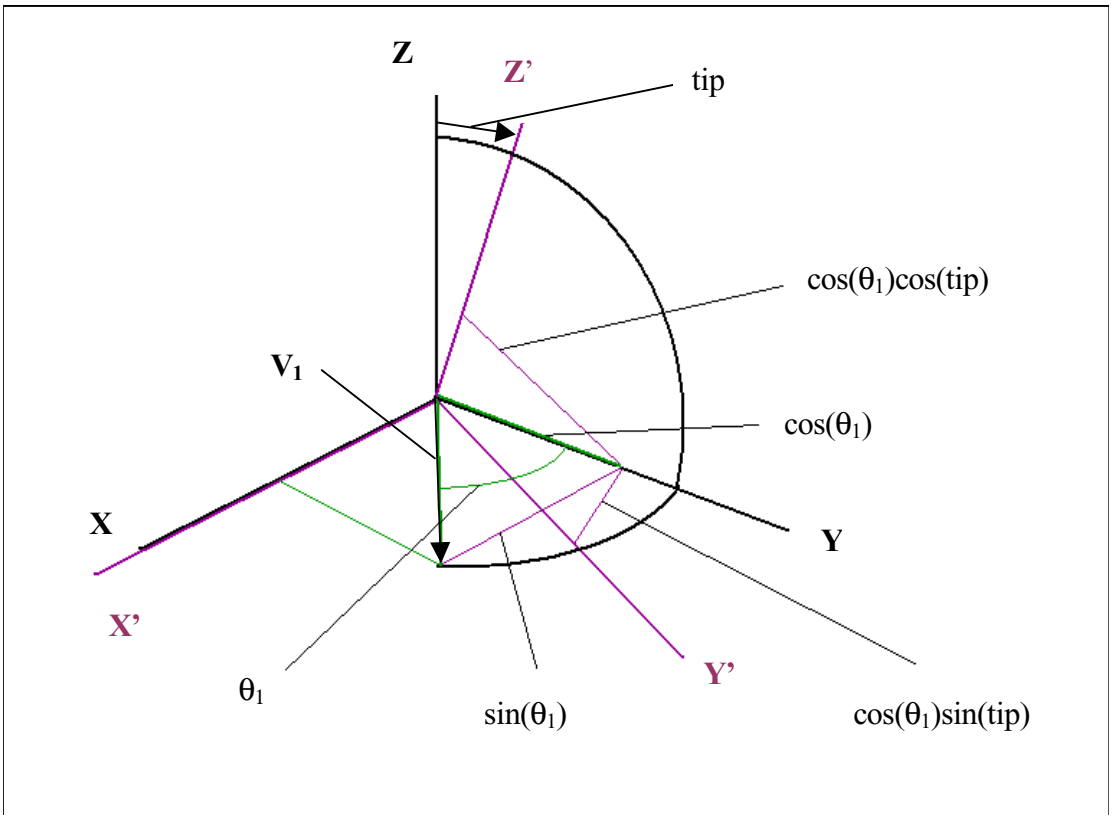

Fig. 22 The unprimed coordinate system in the laboratory and the primed coordinate system in the frame of the sensor head are shown. The center slit is in the Y-Z and the Y'-Z' plane. The primed system is tipped by the angle "tip" toward the Y axis. The light from the collimated beam is swept by in the X-Y plane, and illuminates the center slit on the Y axis and the first slit an angle θ_1 earlier when the vector from the sensor head to the collimator is V_1. (Note that angle θ_1 is negative in Table 11.)

Now the zenith angle and azimuth angles in the coordinate system of the sensor head where the first slit was observed are easily obtained from the components of V_1 in the primed system as

$$ZA_1 = \cos^{-1}[\cos(\theta_1)\ \sin(tip)], \quad (13.)$$
$$AZ_1 = \tan^{-1}[\cos(\theta_1)\ \cos(tip)/\sin(\theta_1)]. \quad (14.)$$

The same relations hold for the zenith angle and azimuth angle at which the third slit is observed with θ_2 substituted for θ_1 in equations (13.) and (14.). With these relations, the difference in the azimuth angle locations of slits1 to 3 and the zenith angles for the observations of slits 1 and 3 can be evaluated from the observations.

Data were collected for a dozen different tip angles corresponding to central zenith angles (ZA) from 25 to 77 degrees at rotation rates of 4 and 20 rpm. The observations are shown in Table 11.

Table 11
Observations to Map Locations of Slits

Central Zenith Angle (ZA)	Down tip angle	20 rpm θ_1	σ	4 rpm θ_1	σ	20 rpm θ_2	σ	4 rpm θ_2	σ
77	13	-3.463	0.012	-3.338	0.013	3.159	0.024	3.290	0.002
75	15	-3.743	0.007	-3.531	0.019	3.408	0.000	3.604	0.005
70	20	-4.295	0.013	-4.147	0.024	4.209	0.003	4.285	0.006
65	25	-4.846	0.037	-4.891	0.042	4.948	0.004	5.007	0.007
60	30	-5.807	0.045	-5.615	0.104	5.618	0.008	5.804	0.023
55	35	-6.653	0.002	-6.501	0.079	6.492	0.021	6.632	0.008
50	40	-7.440	0.049	-7.323	0.018	7.398	0.025	7.506	0.015
45	45	-8.440	0.015	-8.269	0.052	8.180	0.003	8.407	0.020
40	50	-9.147	0.029	-9.031	0.025	9.203	0.033	9.231	0.041
35	55	-9.869	0.024	-9.865	0.024	9.940	0.003	9.956	0.025
30	60	-10.845	0.020	-10.647	0.000	10.522	0.001	10.722	0.000
25	65	-11.439	0.005	-11.310	0.012	11.307	0.045	11.389	0.000

Table 12 shows the reduction of the θ_1 and θ_2 measurements at 4 and 20 rpm to zenith and azimuth angles. It seems that the observations at the two rotation rates give slightly different values for θ_1 and θ_2. However, the difference in the locations of slit 3 and slit 1 are very consistent at the two rotation rates. The zenith angle as a function of the difference in azimuth of slits 1 and 3 for the data of the two rotation rates combined is shown in Fig. 23. This relation is fit by a polynomial as shown in the figure. The residuals from the polynomial fit are shown in Fig. 24. The rms residual is 0.048 degrees in zenith angle.

Thus, the Sun Sensor observations during Titan entry will be used to obtain the apparent zenith angle of the sun throughout the descent. This will be done by smoothly interpolating in the times of the central slit crossing to obtain the period of the rotation at the time of each central slit crossing. Then the difference in azimuth angles from slit 1 to slit 3 will be evaluated from

$$\text{Delta Az} = 360\ (T3 - T1)/\text{Period}. \qquad (15.)$$

The value found for Delta Az will be used in the polynomial fit to determine the local apparent zenith angle of the sun from

$$\text{Zenith Angle} = 111.2 - 6.9029(\text{Delta Az}) + 0.33782(\text{Delta Az})^2$$

$$-0.010091(\text{Delta Az})^3 - 0.0001567(\text{Delta Az})^4 - 9.627\times10^{-7}(\text{Delta Az})^5. \qquad (16.)$$

Table 12
Slit Locations in Zenith and Azimuth

Central Zenith Angle (ZA)	4 rpm Zen 1	4 rpm Az 1	20 rpm Zen 1	20 rpm Az 1	4 rpm Zen 3	4 rpm Az 3	20 rpm Zen 3	20 rpm Az 3	Average Zenith	Average Az 3 – Az 1
77	77.02	-3.43	77.02	-3.55	77.02	3.38	77.02	3.24	77.022	6.799
75	75.03	-3.65	75.03	-3.87	75.03	3.73	75.03	3.53	75.030	7.394
70	70.05	-4.41	70.06	-4.57	70.06	4.56	70.06	4.48	70.057	9.010
65	65.1	-5.39	65.1	-5.34	65.10	5.52	65.10	5.46	65.099	10.858
60	60.16	-6.48	60.17	-6.70	60.17	6.69	60.16	6.48	60.164	13.175
55	55.26	-7.92	55.27	-8.10	55.27	8.08	55.26	7.91	55.263	16.005
50	50.39	-9.52	50.4	-9.67	50.41	9.76	50.40	9.62	50.401	19.288
45	45.59	-11.61	45.62	-11.85	45.61	11.80	45.58	11.49	45.601	23.380
40	40.84	-13.89	40.86	-14.06	40.88	14.19	40.87	14.15	40.862	28.144
35	36.19	-16.87	36.19	-16.87	36.21	17.02	36.21	16.99	36.202	33.872
30	31.67	-20.61	31.73	-20.96	31.69	20.74	31.63	20.38	31.678	41.345
25	27.29	-25.33	27.34	-25.58	27.32	25.48	27.29	25.32	27.309	50.857

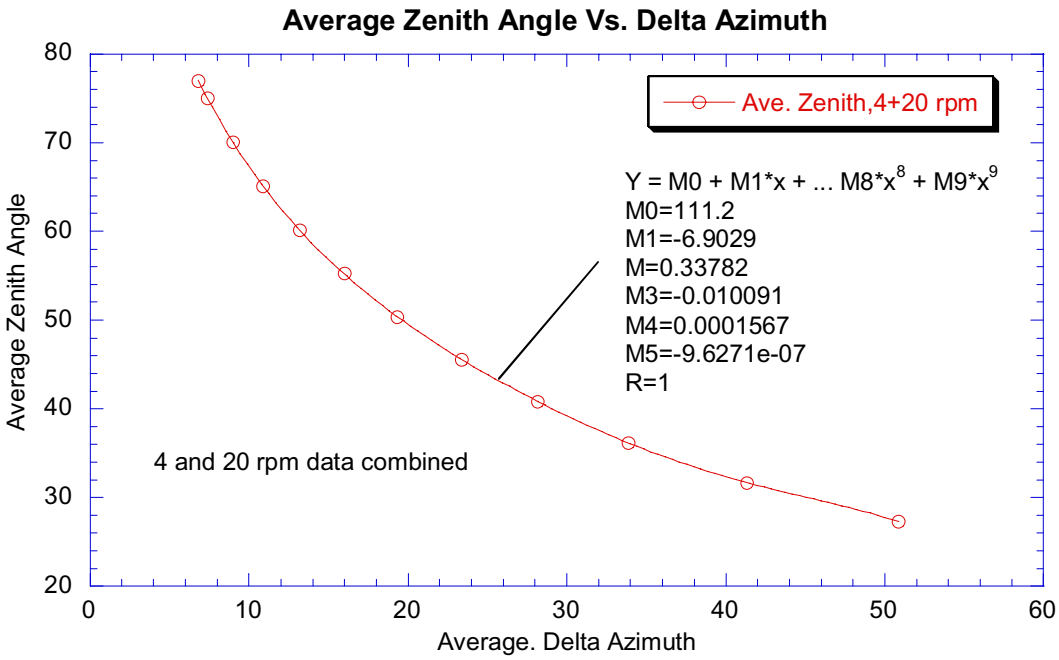

Fig. 23 Average value of zenith angle Vs. average delta azimuth from slit 1 to slit 3 for observations at 4 and 20 rpm combined. The polynomial indicated provides a good fit to the observed relationship.

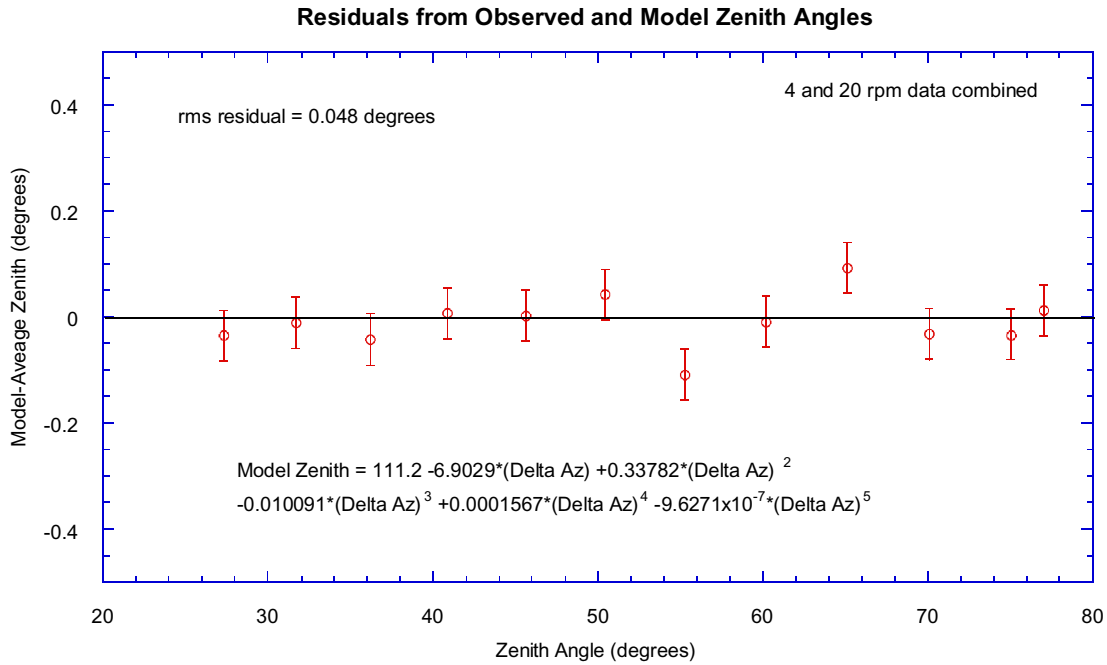

Fig. 24 Residuals from the polynomial fit to the relationship between zenith angle and the difference in azimuth of the first and third slits. The rms residual is 0.048 degrees in zenith angle.

9.0 Relative Spectral Response

The relative spectral response of the SN03 sun sensor was measured at room temperature on September 18, 1996. In this test, we used the monochrometer to illuminate the collimator, and measured the collimated monochromatic beam using the sensor head mounted on the altitude – azimuth mount. The rotating flat mirror device was not used in this test so the sun sensor system could only be read out using the breakout box to pick off the analog signal coming from the sensor head. We monitored the brightness of the collimated monochromatic beam using the standard silicon reference detector. We stepped the monochrometer through wavelengths from 924 to 962 nm in two nanometer steps while we read the analog signal from the sun sensor (in mv) as well as the signal from the standard reference detector. Thus, the relative spectral response of the sun sensor at each wavelength step of the monochrometer is the relative spectral response of the standard detector at that wavelength times the ratio of the sun sensor signal to the signal from the standard detector. These measurements were repeated at five elevation angles as shown in Table 13 below.

Table 13
Observations for Measurements of Relative Spectral Response of Sun Sensor

Wave-length			Ele-vation			Ref. Det. signal	Ref. response
(nm)	17	30	43.1	60	70	(microamps)	(A/W)
924	0.000	-0.142	-0.190	-0.157	-0.150	22.62	0.49878
926	0.156	-0.121	-0.176	-0.147	-0.240	22.31	0.49982
928	2.160	-0.970	-0.159	-0.122	0.661	23.82	0.50085
930	9.490	-0.270	-0.131	0.038	2.430	24.43	0.50189
932	23.100	0.456	-0.740	1.030	5.650	25.04	0.50288
934	43.200	3.560	0.136	3.890	11.040	25.67	0.50387
936	68.500	12.010	1.851	8.960	18.840	26.30	0.50486
938	99.700	27.200	13.040	17.860	30.050	26.96	0.50585
940	140.700	54.400	30.350	34.310	47.130	27.75	0.50684
942	186.900	85.000	36.900	53.590	68.060	28.60	0.50766
944	212.500	97.300	41.600	61.710	79.350	29.53	0.50847
946	209.400	103.900	42.700	64.490	80.010	30.72	0.50929
948	191.900	101.200	41.900	62.900	75.350	31.90	0.51010
950	159.200	86.900	36.000	53.900	63.830	32.44	0.51092
952	115.600	60.400	20.300	39.090	46.500	32.58	0.51143
954	66.300	28.600	8.530	20.120	25.820	32.75	0.51195
956	21.700	7.600	3.690	6.100	8.420	32.93	0.51246
958	3.440	1.430	0.793	1.170	1.340	33.12	0.51297
960	0.330	0.084	-0.071	0.017	0.025	33.32	0.51348
962	0.000	-0.147	-0.190	-0.173	-0.167	33.53	0.51377

We took the mean of the readings at wavelengths of 924 and 962 nm as the bias level of the readings at each elevation. The readings minus the bias times the relative spectral response of the reference detector divided by the signal from the reference detector give the relative spectral response at each elevation angle as a function of wavelength. Normalizing to a maximum reading of 1.00 at the peak response at each elevation gives the results in Table 14.

Table 14
Relative Spectral Response of Sun Sensor vs. Elevation Angle

Wavelength (nm)	Elevation = 17	Elevation = 30	Elevation = 43.1	Elevation = 60	Elevation = 70
924	0.0000	0.0000	0.0000	0.0002	0.0001
926	0.0010	0.0003	0.0004	0.0004	-0.0013
928	0.0124	-0.0101	0.0009	0.0008	0.0126
930	0.0533	-0.0015	0.0017	0.0039	0.0388
932	0.1268	0.0070	-0.0154	0.0224	0.0852
934	0.2317	0.0422	0.0089	0.0743	0.1606
936	0.3594	0.1353	0.0544	0.1634	0.2664
938	0.5113	0.2974	0.3450	0.3155	0.4140
940	0.7023	0.5776	0.7752	0.5874	0.6309
942	0.9067	0.8762	0.9149	0.8902	0.8845
944	1.0000	0.9727	1.0000	0.9940	1.0000
946	0.9488	1.0000	0.9882	1.0000	0.9708
948	0.8387	0.9395	0.9353	0.9408	0.8820
950	0.6853	0.7948	0.7921	0.7944	0.7361
952	0.4959	0.5510	0.4470	0.5749	0.5350
954	0.2832	0.2605	0.1894	0.2958	0.2966
956	0.0923	0.0699	0.0839	0.0910	0.0975
958	0.0146	0.0141	0.0212	0.0193	0.0170
960	0.0014	0.0020	0.0025	0.0026	0.0021
962	0.0000	0.0000	0.0000	-0.0001	-0.0001

These curves of observed relative spectral response at five elevation angles at room temperature are shown in Fig. 25.

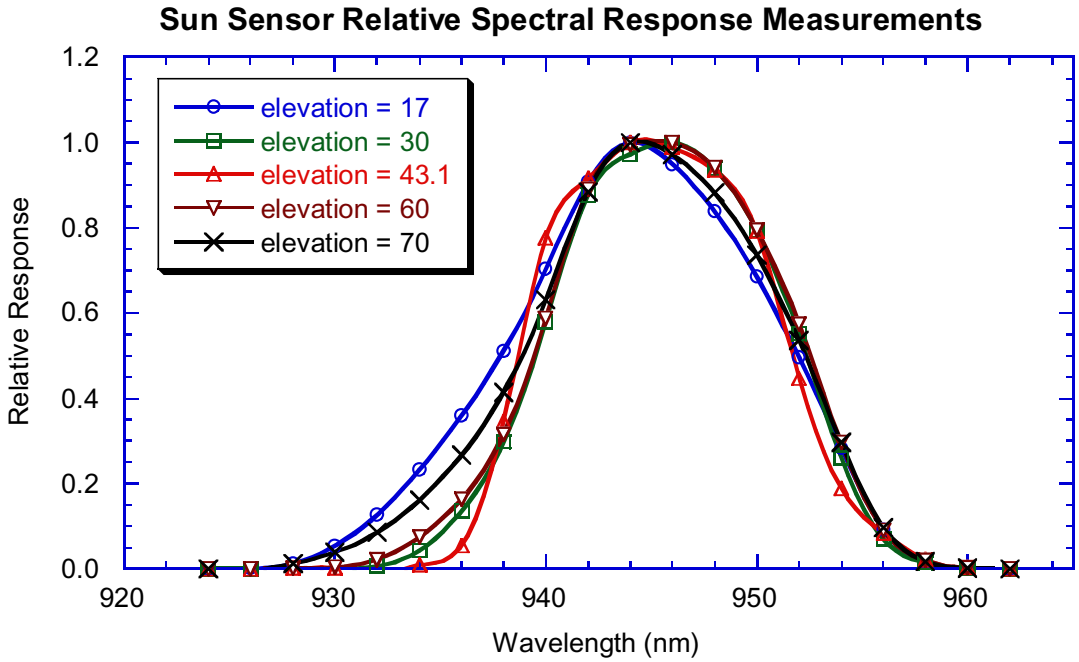

Fig. 25 Measurements at room temperature of the relative spectral response of the sun sensor of the DISR flight model as a function of wavelength are shown at five different elevation angles, as labeled.

It is useful to have an analytic expression that gives the shape of the relative spectral response as a function of elevation angle. In view of the asymmetry in the spatial response function at some elevation angles, we use different parameters for the part of the spectral response function shortward of the peak and longward of the peak response. We used the following form for the spectral response function:

$$R_2(\lambda) = \exp(-[(\lambda-\lambda_c)/(\lambda_2-\lambda_c)]^{P2}) \qquad (17.)$$

For the spectral response when $\lambda > \lambda_c$, the central wavelength, and

$$R_1(\lambda) = \exp(-[(\lambda-\lambda_c)/(\lambda_1-\lambda_c)]^{P1}) \qquad (18.)$$

When $\lambda < \lambda_c$. Here λ_1 and λ_2 control the width of the two halves of the spectral response function, and the powers P1 and P2 control the sharpness of the fall off of these two tails. We find the following values of these parameters at the five elevation angles measured as shown in Table 15.

The shapes measured for the relative spectral response at each elevation angle are compared to the model spectral response functions in Figs. 26 below.

Table 15
Values of Spectral Response Function Parameters at Measured Elevation Angles

Elevation (degrees)	17	30	43.1	60	70

P1	1.7	2.5	3.6	2.1	1.6
λ_1(nm)	936.3	938.5	938.1	938.3	937.3
λ_c(nm)	944.2	945.0	944.8	944.7	944.1
λ_2(nm)	953.0	953.2	952.8	953.5	953.2
P2	2.5	3.0	3.1	3.1	2.8
Rms residual	0.019	0.012	0.019	0.014	0.014

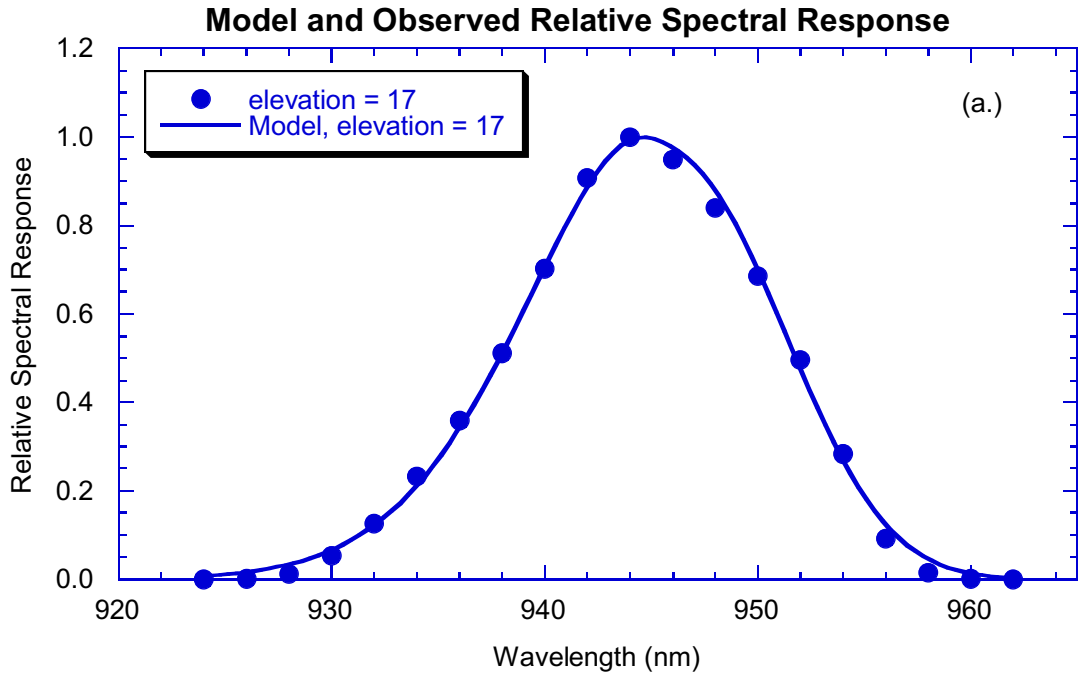

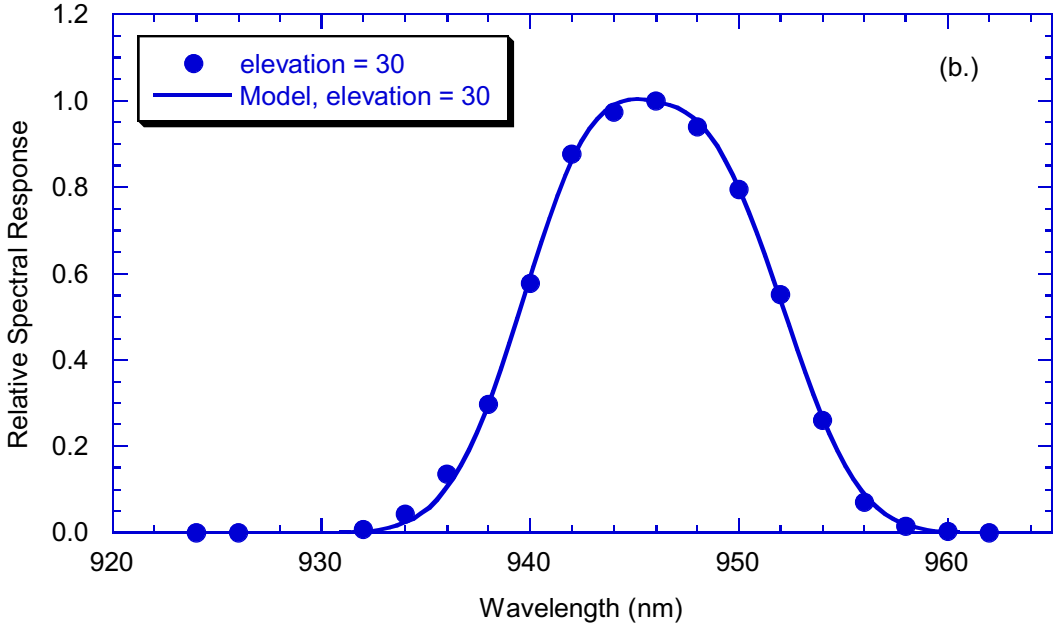
elevation = 30
Model, elevation = 30
(b.)
Relative Spectral Response
Wavelength (nm)
1.2
1.0
0.8
0.6
0.4
0.2
0.0
920
930
940
950
960

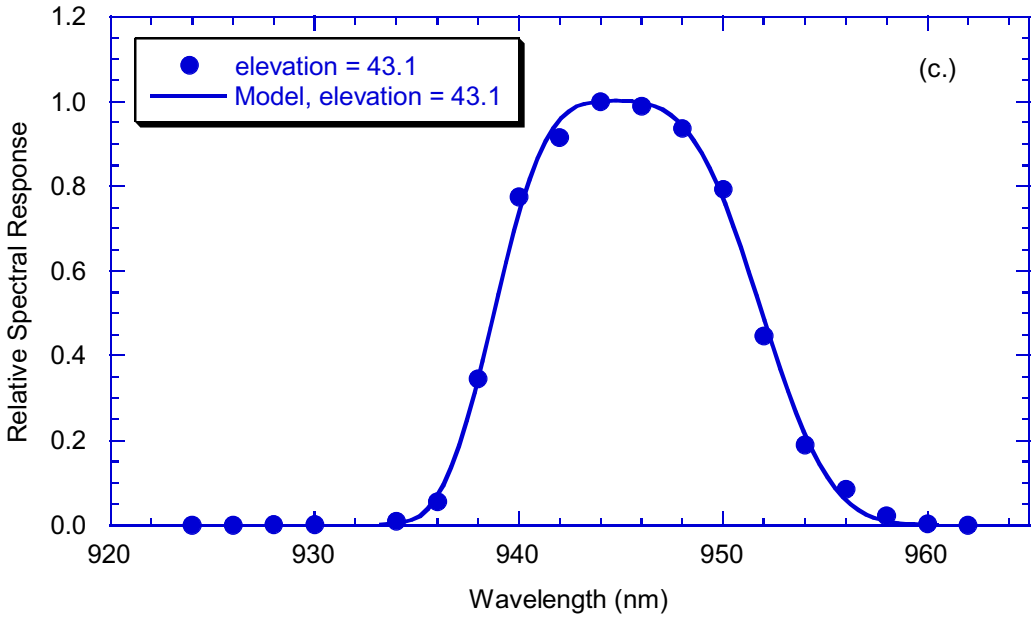
elevation = 43.1
Model, elevation = 43.1
(c.)
Relative Spectral Response
Wavelength (nm)
1.2
1.0
0.8
0.6
0.4
0.2
0.0
920
930
940
950
960

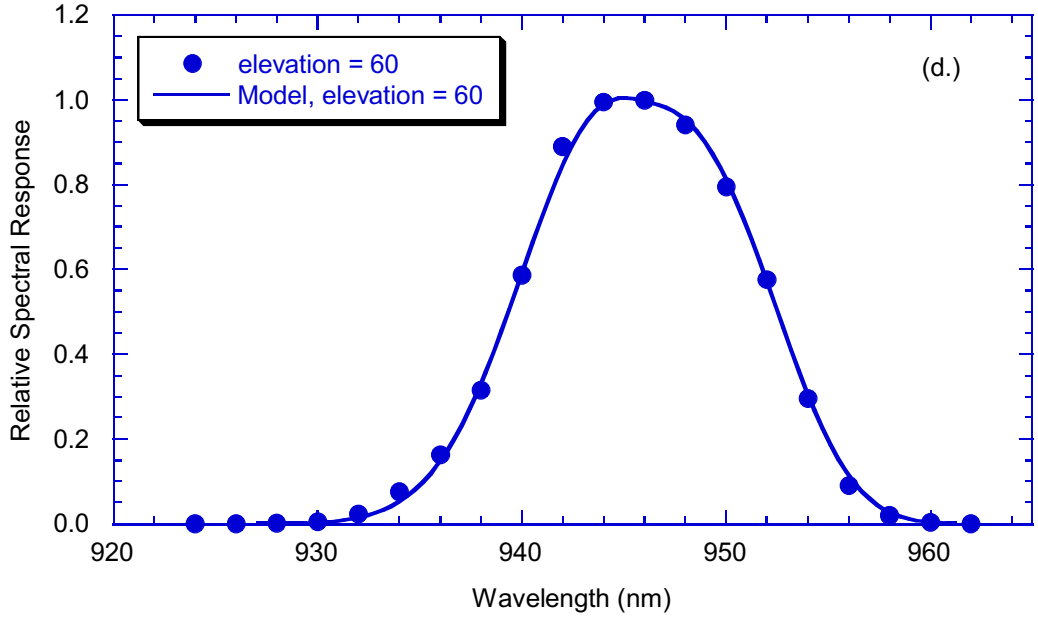

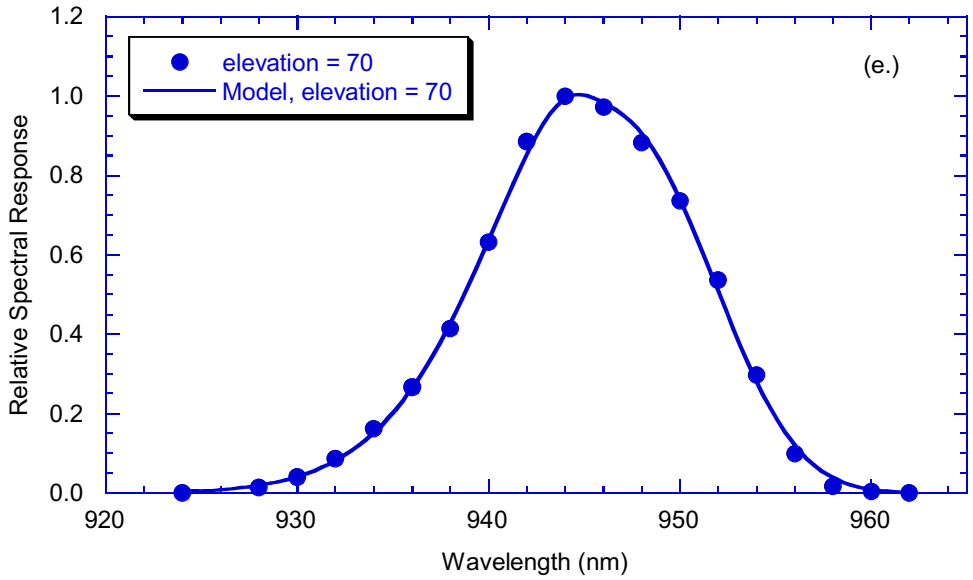

Fig. 26 The observed spectral response values (points) are shown as functions of wavelength at each of five elevation angles in panels (a.) through (e.), as labeled. The model spectral response values computed from the parameters in Table 16 using the expressions in equations (17.) and (18.) are shown by the smooth curves in each panel. The models and observations agree to rms residuals of < 2% in each case.

Finally, the parameters in Table 15 can be plotted against elevation angle and fitted to polynomial expressions to permit the relative spectral response to be obtained at any elevation angle. The model parameters are shown in Fig. 27. The curves in Fig. 27 are fit by polynomials in elevation angle, or

$$\text{Param(el)} = m0 + m1*el + m2*el^2 + m3*el^3 + m4*el^4. \quad (19.)$$

Where el represents the elevation angle in degrees. The coefficients m of the polynomial fits to each parameter are given in Table 16.

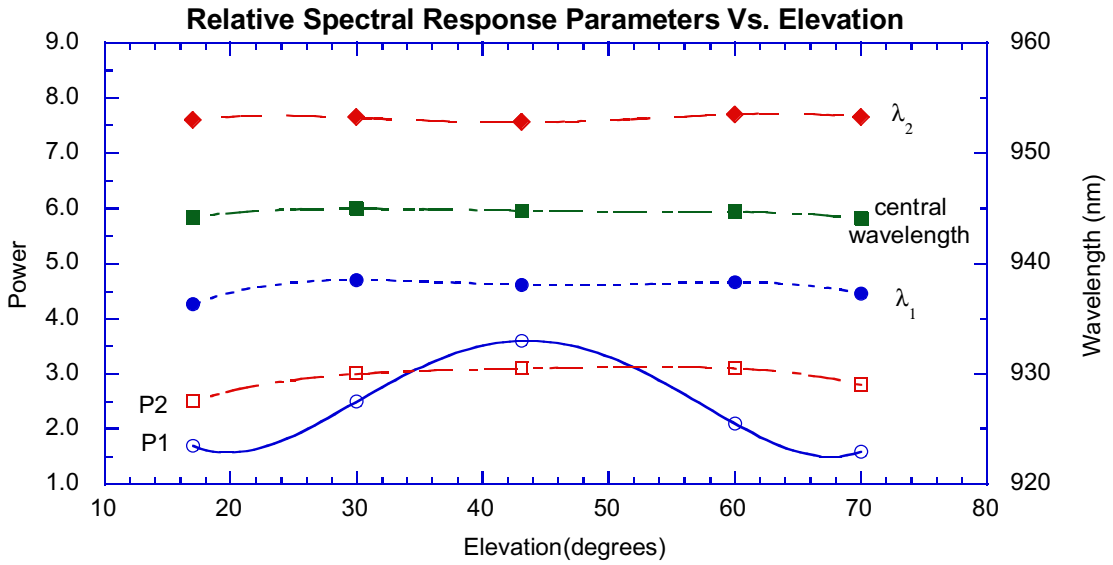

Fig. 27 Relative spectral response parameters are plotted as a function of elevation angle. The polynomial fits are given in Table 16.

Table 16
Polynomial Fit Coefficients to Relative Spectral Response Parameters

Parameter	m0	m1	m2	m3	m4
P1	12.782	-1.4658	0.064748	-1.0994e-3	6.2989e-6
λ_1(nm)	916.17	2.2138	-0.07911	1.2023e-3	-6.6055e-6
λ_c(nm)	936.66	0.83117	-0.029803	4.5447e-4	-2.5235e-6
λ_2(nm)	944.17	1.076	-0.043893	7.2836e-4	-4.2083e-6
P2	-0.3017	0.29012	-0.0095768	1.4353e-4	-8.1266e-7

The parameters in Table 16 together with equations (17.), (18.), and (19.) permit the relative spectral response to be evaluated at any elevation angle. Figure 28 shows relative spectral response curves computed at 7 elevation angles from 17 to 70 degrees.

The model of the relative spectral response function can be integrated to give the equivalent width of the sun sensor bandpass as a function of elevation. The results of integrating the model as well as the result of integrating the directly measured relative spectral response are shown as functions of elevation angle in Fig. 29. Note that the equivalent width can be described as a polynomial in elevation angle as

$$\text{E.W.(nm)} = 25.843 - 1.1257*el + 0.036127*el^2 - 5.025\text{x}10^{-4}*el^3 + 2.6035\text{x}10^{-6}*el^4. \quad (22.)$$

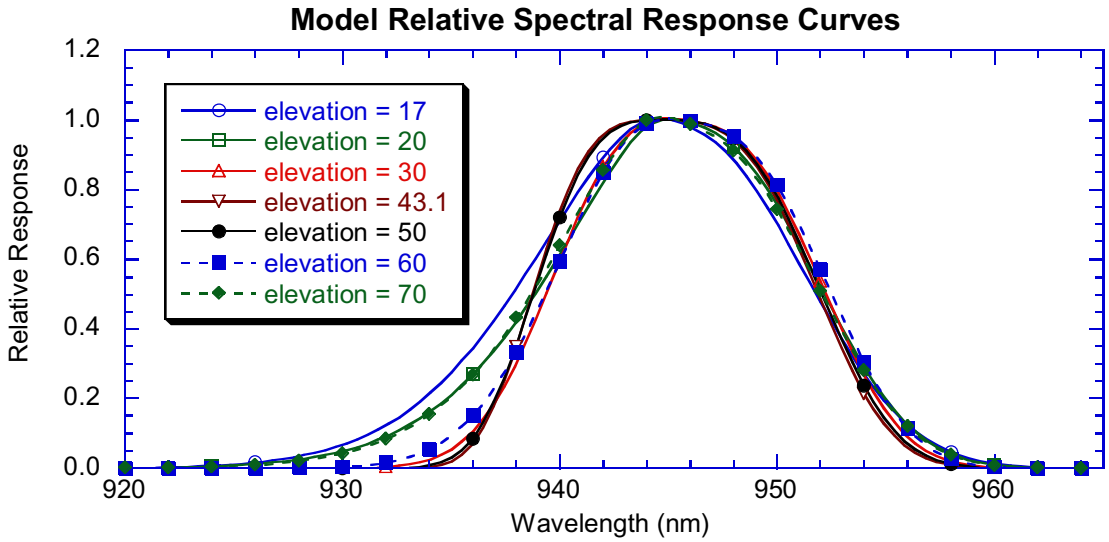

Fig. 28 Model spectral response curves computed at seven elevation angles using the parameters of Table 17.

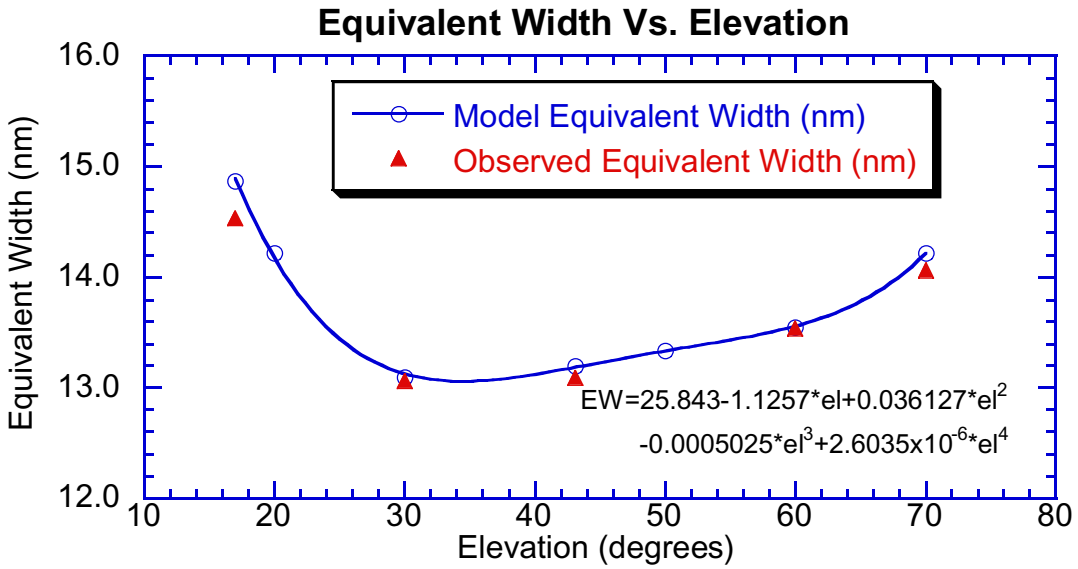

Fig. 29 Equivalent width (nm) plotted as a function of elevation angle. The results of integrating the model are shown by the circles, while filled triangles show the results of integrating the measured spectral response. The polynomial gives the result of fitting the model values.

10.0 Software

The filtered silicon detector of the sun sensor continuously produces an analog signal as the probe rotates and descends throughout the mission. The analog signal from

the sun sensor is converted to a digital signal using a 12-bit analog to digital (A/D) converter. Based on the average of the peak values from the three pulses observed on the last rotation, a digital threshold value is set for the following rotation. This value is converted to an analog signal using an 8-bit digital to analog (D/A) converter, and the comparison is done in analog electronics. The instrument clock is read when the analog signal from the sun sensor crosses the threshold level on the leading edge and trailing edge of the signal from each slit. The average of the leading edge and trailing edge times from each pulse are included in the telemetry stream. The optical depth of the Titan atmosphere at the near infrared continuum wavelength of the sun sensor is expected to be modest (near unity), but will not be well known at the entry site before the mission. The dynamical updating of the threshold during the descent improves the behavior of the sun sensor system and prevents triggering on possible patches of cloud in the atmosphere. Ideally, we would have wanted the threshold value to be about half the brightness of the pulses on the last rotation. However, because the D/A converter has only 8 bits while the A/D converter has 12 bits, some compromise is necessary. We have chosen to keep the ratio near 0.5 throughout most of the dynamic range of the instrument, and to fix the threshold value at a signal value of 423 DN (about 10% of full scale) for sun sensor data values above 846 DN. When the sun sensor signal falls below 846 DN, the threshold value is adjusted down (at the resolution of the D/A converter) to stay about 0.5 times the sun sensor data number. This behavior is shown in Fig. 30.

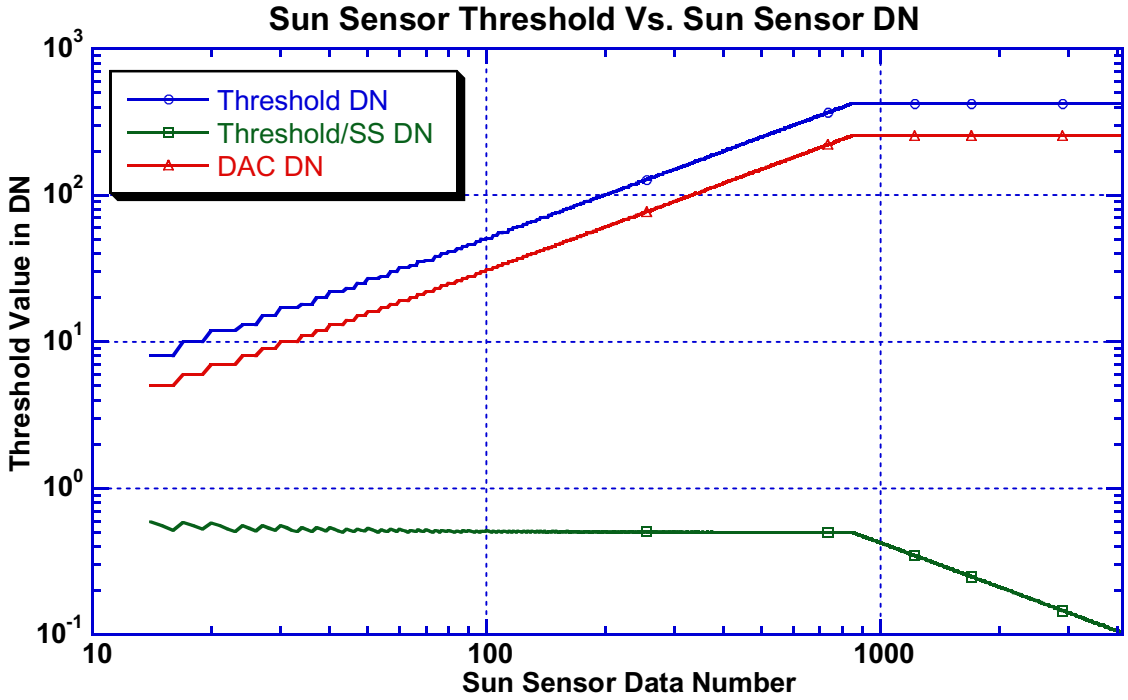

Fig. 30 The value of threshold level produced by the D/A converter is shown as a function of the sun sensor data number. The corresponding value of the threshold in sun sensor units is shown as the threshold DN. The ratio of the threshold value to the sun sensor data number is shown also. This ratio is about 0.5 for sun sensor data numbers below 846 DN, and drops to about 10% of the sun sensor data number at full scale of the sun sensor.

The dynamic adjustment of the sun sensor threshold automatically prevents pulses with a height less than the threshold value from being detected throughout the descent. This is not the only feature included to prevent triggering the sun sensor on signals from possible patches of bright cloud during the descent. Knowledge of the small size of the disk of the sun at Titan and the width and location of the slits leads to predictions about the distribution of the times of the triplets of pulses expected from the sun. Four additional criteria are required for pulses to be accepted as valid sun pulses. First, for valid sun pulses, the gap between the first and second pulses of a triplet must be nearly the same as the gap between the second and third pulses of a triplet. We require that the difference in these two gap times divided by the average of the gap times be less than 0.268. Table 17 summarizes the measurements of the gap times made during calibration and insures that this criterion will be met over the full range of zenith angles of the sun sensor. We see from our measurements that this value for the flight instrument should not exceed 0.1, including a reasonable margin of safety against rejecting valid triplets.

Also shown in Table 17 are two additional criteria for valid sun pulses. We require that the average gap between the first and second and the second and third pulses exceeds the average width of each pulse (obtained from the rising and falling edge times) by a factor of 2.2 or greater. Figure 12 above shows that the full width at half maximum of the pulse from the disk of the sun at Titan is expected to be about 0.25 degrees. The full width at 0.1 times the maximum signal is expected to be 0.375 degrees. The width in azimuth will be these widths in angle divided by the sine of the solar zenith angle. The table shows that the ratio of average gap size divided by average pulse width is expected to be at least 8.4 at Titan entry, and so includes a fair margin of safety against rejecting valid triplets.

We also require that the time between the center pulses of two successive triplets be greater than the average of the two gap times of the first triplet by a factor greater than or equal to 5. Table 17 shows that this factor is at least 14 for the flight unit. Again a fair margin of safety is available to prevent rejection of valid triplets during the descent.

Table 17
Criteria for Valid Triplets vs. Solar Zenith Angle

Zenith angle (degrees)	Gap 1 at 4 rpm	Gap 2 at 4 rpm	Difference in gap/ ave gap	Gap 1 at 20 rpm	Gap 2 at 20 rpm	Difference in gap/ ave gap	Min gap/max Width	Period/ max gap
77	3.43	3.38	0.015	3.55	3.24	0.091	8.42	101.4
75	3.65	3.73	0.022	3.87	3.53	0.092	9.09	93.0
70	4.41	4.56	0.033	4.57	4.48	0.020	11.05	78.8
65	5.39	5.52	0.024	5.34	5.46	0.022	12.91	65.2
60	6.48	6.69	0.032	6.70	6.48	0.033	14.96	53.7
55	7.92	8.08	0.020	8.10	7.91	0.024	17.28	44.4
50	9.52	9.76	0.025	9.67	9.62	0.005	19.45	36.9
45	11.61	11.8	0.016	11.85	11.49	0.031	21.67	30.4
40	13.89	14.19	0.021	14.06	14.15	0.006	23.81	25.4
35	16.87	17.02	0.009	16.87	16.99	0.007	25.80	21.2
30	20.61	20.74	0.006	20.96	20.38	0.028	27.17	17.2
25	25.33	25.48	0.006	25.58	25.32	0.010	28.54	14.1
Limit criterion			< 0.268			< 0.268	> 2.2	> 5

The final criterion for valid triplets is that the width of each of the three pulses in a triplet must be equal to within a factor of 1.5. The width of the pulses can be slightly different due to the fact that the optical aberrations vary somewhat with position in the optical field of view of the sun sensor depending on the distance from the optical axis. Also, the two side slits are tipped somewhat, increasing the distance across these slits. Nevertheless, the main contribution to the width of the pulses from the small disk of the sun at Titan will be the width of the slits, fixed at 0.25 degrees. In the focal plane, the first and third slits are only tipped by 9 degrees from the center vertical slit, so the distance across these slits is greater than the distance across the center slit by only 1%. The factor of 1.5 seems relatively safe also.

The sun sensor operates in four distinct states: 1) initial; 2) search; 3) initial detection; and 4) locked. The sun sensor begins in the initial state. The sun sensor enters the search state if either the mission time is greater than the probe mission timeout value of 2 minutes or the DISR master time is greater than the DISR elapsed timeout value of 2 minutes.

Upon entry into search mode, the software determines a search time as the time required for 4 complete rotations of the probe based on the probe broadcast spin information but never less than 10 seconds and never more than 2 minutes.

If valid pulses are detected, the initial detection mode is entered. In this case the threshold value is set to the maximum sun sensor response multiplied by the threshold factor. An initial detection time is set as the time for 8 complete rotations of the probe based on the probe broadcast spin information but never less than 20 seconds or more than 4 minutes. The sun sensor remains in the initial detection state until either the initial detection time has elapsed in which case the search mode is restarted, or at least 5 consecutive sun pulses meet all criteria for valid pulses in which case the locked mode is entered.

The sun sensor remains in the locked mode until either the received sun pulses fail a validity check, or the threshold values is less than or equal to the minimum valid peak solar signal, or no valid triplets are received for the time predicted for two full rotations based on the previous valid triplet. In these cases, the sun sensor returns to the search mode.

The software uses the azimuth and spin rate from the sun sensor while in the locked mode, or from the probe broadcast information if not in the locked mode. In either case, the azimuth for the next rotation is assumed to be a quadratic extrapolation based on the times of the center pulse crossings of the last three valid triplets. When the system changes from using valid triplets from the sun sensor to probe broadcast values for determining azimuth, the current azimuth is determined from the most recent valid sun pulse data.